

UHASSELT



Maastricht University

KNOWLEDGE IN ACTION

Faculty of Medicine and Life Sciences School for Life Sciences

Master of Biomedical Sciences

Master's thesis

Advanced Silica Nanoparticles: Relations between Synthesis, Morphology, and Toxicology

Carmen Smeets

Thesis presented in fulfillment of the requirements for the degree of Master of Biomedical Sciences, specialization Bioelectronics and Nanotechnology

SUPERVISOR :

Prof. dr. An HARDY

MENTOR :

Mevrouw Ulrique VOUNCKX

Transnational University Limburg is a unique collaboration of two universities in two countries: the University of Hasselt and Maastricht University.



UHASSELT

KNOWLEDGE IN ACTION

www.uhasselt.be
Universiteit Hasselt
Campus Hasselt:
Martelarenlaan 42 | 3500 Hasselt
Campus Diepenbeek:
Agoralaan Gebouw D | 3590 Diepenbeek

2021
2022



UHASSELT

KNOWLEDGE IN ACTION



Maastricht University

Faculty of Medicine and Life Sciences

School for Life Sciences

Master of Biomedical Sciences

Master's thesis

Advanced Silica Nanoparticles: Relations between Synthesis, Morphology, and Toxicology

Carmen Smeets

Thesis presented in fulfillment of the requirements for the degree of Master of Biomedical Sciences, specialization Bioelectronics and Nanotechnology

SUPERVISOR :

Prof. dr. An HARDY

MENTOR :

Mevrouw Ulrique VOUNCKX

Advanced Silica Nanoparticles: Relations between Synthesis, Morphology, and Toxicology*Carmen Smeets¹, Ulrique Vounckx^{1,2,3}, Nelly Saenen⁴, Marlies Van Bael^{1,2,3}, and An Hardy^{1,2,3},¹Materials Chemistry, Hasselt University, Institute for Materials Research (IMO-IMOMECE), DESINE Group, Agoralaan Building D, 3590 Diepenbeek, Belgium²Energyville 2, Thor park 8320, 3600 Genk, Belgium³IMEC division, IMOMECE, Wetenschapspark 1, 3590 Diepenbeek, Belgium⁴Zoology: Biodiversity and Toxicology (CMKDK), Hasselt University, Centre for Environmental Sciences (CMK), Agoralaan Building D, 3590 Diepenbeek, Belgium*Running title: *Advanced Silica Nanoparticles*

To whom correspondence should be addressed: Prof. dr. An Hardy, Tel: +32 (11) 26 83 08; Email: An.Hardy@uhasselt.be

Keywords: silica, nanoparticles, multilamellar, PMOs, sol-gel synthesis, cytotoxicity**ABSTRACT**

Mesoporous silica nanoparticles are currently being explored as drug delivery systems, but are not optimized yet for a wide variety of drugs. In this project, we propose the use of multi-shelled periodic mesoporous organosilica (PMO) spheres as a novel and improved drug delivery system. We hypothesized that by optimizing the PMO synthesis, a more suitable nanoparticle for drug delivery could be created in comparison to conventional PMOs. PMOs with one or two layers were synthesized via sol-gel synthesis, guided by a surfactant template. Hydrothermal treatment resulted in a structural transformation to hollow-core PMOs. The morphology was analyzed using physicochemical analysis. The PMOs had a diameter ranging between 200 and 300 nm. Mesoporosity was confirmed using nitrogen sorption analysis. In water, all PMOs were stable, with a high negative zeta potential. However, in other media, hollow-core PMOs had a higher tendency to agglomerate. Additionally, cytotoxicity was assessed after 24 hours of exposure. Single-shell PMOs did not alter cell viability significantly. Cells exposed to double-shell PMOs showed a slight increase in metabolic activity, ROS production, and LDH release at higher concentrations when compared to non-exposed cells. Although further studies on stability, functionalization, and loading are needed, these PMOs are shown to be promising candidates as a drug delivery system due to their easy and tunable

synthesis, large mesoporous volume for drug loading, and biocompatibility.

INTRODUCTION

Silicon dioxide (SiO₂), most commonly referred to as silica, is a frequently used material in many fields. It occurs in either a crystalline or an amorphous form (1). Whereas crystalline silica is naturally prevalent in quartz, tridymite, and cristobalite, amorphous silica is mostly present in obsidian and opals (1, 2). Besides being a naturally occurring product, synthetic silica is also produced in many industries. Due to it being a biocompatible and biodegradable material in its amorphous form, the use of silica in the medical field has been increasing, with examples including bone and tooth implants, scaffolds, and as a candidate for therapeutics and diagnostics (2-4). At the nanoscale, **silica nanoparticles (SiNPs)** gain additional attractive properties compared to their larger bulk counterpart. Nanoparticles are generally defined by their size within the nanometer range, which leads to a higher surface-to-area ratio and a higher surface reactivity (1, 3, 4). SiNPs in particular have been used in many industries, most notably as an additive to cosmetics and varnishes to prolong their lifetime (1). These SiNPs can be formed via multiple techniques, e.g. Stöber synthesis, sol-gel synthesis (a modified version of the Stöber method), reverse microemulsion, and flame synthesis (5, 6). The resulting SiNPs are either solid or mesoporous, with the latter being

characterized by a tunable pore size varying between 2 and 50 nm (3, 7). These **mesoporous silica nanoparticles (MSNs)** were first described by the Mobil Research and Development Corporation in 1992 as Mobil Composition of Matter 41 (MCM-41), a part of the “ordered mesoporous molecular sieves” family (6, 8, 9). These MCM-41 were synthesized using a liquid crystal templating mechanism, which is similar to the aforementioned sol-gel method (8, 9). Many MSNs have shown to be rather useful in **biomedical applications**. They are generally used as scaffolds for tissue engineering (3), as imaging agents due to their loading capacity and stability in bioimaging (10), and as a drug delivery system in stem cell research and cancer research (3). Currently, these MSNs are also being investigated as nanocarriers, with promising results. They can be loaded with various substances, such as imaging agents (10) but also therapeutic agents (3, 11). The silica surface is however hydrophilic, resulting in difficulties when trying to load these MSNs with hydrophobic agents (3). Consequently, a higher dose of the loaded MSNs would have to be administered to a patient to elicit the desired therapeutic effect (3). There is thus a clear need for optimized drug delivery systems. In our research, we propose the use of **multi-shelled periodic mesoporous organosilica (PMO) hollow spheres** as a novel and improved drug delivery system. PMOs are organic-inorganic nanocomposites, consisting of inorganic siloxane domains covalently linked by organic functional groups (12-14). These PMOs can be formed either by a single-step or a multi-step process. The latter gives more control over the synthesis of each layer, allowing the formation of various morphologies optimized for the desired application. The PMOs in this project will be synthesized via a multi-step **sol-gel method** (Fig. 1), using the silica precursors tetraethoxysilane (TEOS) and bis(triethoxysilyl)ethane (BTSE), with the surfactant cetyltrimethylammonium bromide (CTAB) as a structure-directing agent (15-17). This bottom-up, wet-chemical technique is an easy-to-use and quick method that allows great control of the synthesis properties (2). As mentioned previously, this method is a modified version of the Stöber synthesis. In the Stöber synthesis, silica precursors are hydrolyzed in alcohol. The formed ethoxysilanols undergo a condensation reaction,

leading to cross-linking of the hydrolyzed precursors (6, 18). In the modified Stöber synthesis, surfactants are added as structure-directing agents (6). The surfactants are dissolved in water and/or alcohol and will form micelles, serving as a template during the synthesis. Next, precursors will be added to the mixture to form the nanoparticle around the surfactant template via hydrolysis and condensation. Afterwards, the nanoparticles can be treated hydrothermally to create hollow-core PMOs. The template can be removed via either solvent extraction or calcination. It should be noted that the use of calcination can result in the removal of the organic groups within the structure, and can only be used when these groups are thermally stable. Additional layers are created by repeating the addition of the precursors before exposing the PMOs to a hydrothermal reaction to transform the layers into hollow shells. The combination of both TEOS and BTSE is favored, as using either of them on their own would not result in the desired nanoparticle morphologies. Only using TEOS would result in a particle without a hollow core, which would readily dissolve during the hydrothermal treatment due to its low condensation degree (15, 19). The use of solely BTSE would result in a solid particle, lacking the desired hollow cavity (15).

The surface of each shell can be **functionalized** during the synthesis itself or by post-synthesis modifications (20). This way, a nanoparticle suitable for the desired loading of a drug can be created. Whereas synthesis using the proposed precursors will result in hydroxylated (-OH) end groups, different silica precursors can be used during the synthesis to incorporate other functional end groups on the silica layers, a process called co-condensation (21-23). Examples of these silica precursors include (3-aminopropyl)-triethoxysilane (APTS), (3-mercaptopropyl)-trimethoxysilane (MPTS), and vinyltriethoxysilane (VTES), which all can be incorporated during the synthesis to functionalize the silica surface, resulting in amino- (R-NH₃), thiol- (R-SH), and alkene (R=CH₂) groups respectively (20, 22, 24). Functionalization of the surface can further be achieved post-synthesis via grafting or surface modifications (21). If the desired surface modifiers are not compatible with the synthesis chemistry, grafting is preferred as a functionalization strategy (21, 23, 25). This method can also be used to coat

the surface with the previously mentioned precursors. The major downsides of this strategy are the inhomogeneous coating of the surface, as well as only coating of the outer surface and not functionalization of the whole structure (23). The other method of functionalization is the modification of the surface with various coating molecules, the most common being polyethylene glycol (PEG). PEG-coatings can be introduced onto the nanoparticle surface by either covalent bonds, physical adsorption, or within the surface (21). These type of coatings are generally used to increase the stability in biological fluids, as it reduces aggregation, improves biocompatibility, and increases the circulation time of nanoparticles (21, 23).

The rationale to use PMOs stems from the use of **multi-shell nanoparticles**. Multi-shell nanoparticles have been investigated with a wide variety of materials, with many applications being related to increasing energy storage, including solar cells (26, 27), lithium-ion batteries (28, 29), supercapacitors (30, 31), sensors (26, 32), and photocatalysis (33, 34). These multi-shell structures have a higher energy loading capacity compared to their single-shell counterpart. It is worth looking into if this increased loading capacity is also translatable to drug loading, as this would make them interesting candidates as a drug delivery system. Hypothetically, the additional layers can contribute to an increased loading capacity, as each layer can be loaded with drugs and subsequently increase the total drug taken up by the PMO. Initial studies describe the synthesis of multi-shell mesoporous silica nanospheres, as well as loading them with the model drugs doxorubicin (35) and ibuprofen (36).

There are **various methods to load** these drugs within mesoporous nanoparticles. The most common methods, e.g. adsorption, incipient wetness, and solvent evaporation methods, make use of an organic solvent, although methods exist that do not rely on a solvent to load the nanoparticles, e.g. physical mixing, melting, or co-milling (37). In the adsorption method, nanoparticles are immersed in a solvent containing a known concentration of the desired loading drug. The pores will be filled via capillary action, after which the nanoparticles will be collected via centrifugation and washed (37, 38). The choice of solvent in this method has to be taken into account.

For SiNPs, the use of non-polar solvents often results in higher concentrations of the drug loaded within the nanoparticles, as polar solvents tend to compete for adsorption sites on the hydrophilic silica surface and thus limit drug adsorption (37). While this method is applicable to a wide variety of drugs, a large amount of the drug is lost during the centrifugation process (37, 38). Many common drugs, e.g. the anticonvulsant drug Carbamazepine (39), and the non-steroidal anti-inflammatory drugs Ibuprofen (40) and salicylic acid (Aspirin) (41, 42), have successfully been loaded within SiNPs using this method. In the incipient wetness impregnation method, a solution containing a known drug concentration is added dropwise to the nanoparticles. Capillary action then fills the pores (37). This method uses a smaller amount of drug in comparison to the adsorption method, making it suitable for more expensive materials (37, 38). Similar to the absorption method, the loading of Carbamazepine (43) and Ibuprofen (44, 45) using this method has been demonstrated before. Lastly, in the solvent evaporation method, SiNPs are added to a solution containing a known concentration of a drug. The solvent used for this method has to be volatile so it can be evaporated, resulting in loaded nanoparticles (37). As with the previous methods, Carbamazepine (46) and Ibuprofen (45) have been loaded within SiNPs, as well as the loop diuretic drug Furosemide (47). Most methods rely on the migration of the drug in the mesopores of the nanoparticles. This can result in premature release of the drug within the body, as the drug can freely migrate out of the particle if the right conditions are met.

The ultimate goal of these PMOs is their application as a drug delivery system. Drug delivery systems are classified based on their delivery routes, which include oral, transdermal, and parenteral routes. **The oral delivery route** is one of the most common routes, as this route allows control over the delivery, ease of administration, and compliance of the patient (48). In contrast, delivery via the transdermal or parental route tends to be less controlled or more invasive. Oral drug delivery systems have to pass a wide variety of barriers to be absorbed. The first major barrier is the acidic environment in the stomach. The presence of many digestive enzymes, in addition to the low pH, may degrade the system and/or its content before it reaches the intestine (48, 49). To ensure the system

and its content stay intact, surface modification or encapsulation can be explored to protect the system. Another important barrier to cross is the uptake of the particle by the intestinal cells. There are two main routes by which a foreign body will be taken up, the transcellular and paracellular routes. In the transcellular route, particles are taken up by the enterocytes, whereas in the paracellular route, particles are transported through the tight junctions between the cells (48, 49). Which route a particle will take is dependent on its size and characteristics, as larger particles like nanoparticles, vesicles, and hydrophobic drug molecules prefer the transcellular route, whereas small hydrophilic drug molecules prefer the paracellular route (48, 50).

With the application of these PMOs as a drug delivery system in mind, **biosafety** should be taken into account. As mentioned previously, silica exists in two main compositions, crystalline and amorphous. **Crystalline silica** and its toxicological effect have been studied extensively. Exposure to this polymorph often occurs in occupations where there is a high prevalence of fine silica particles, for example in drilling or mining operations (51). Health effects of this polymorph are associated with silicosis, a fibrotic lung disease where phagocytosis of the silica particles in the lung causes lysosomal damage and triggering of an inflammatory response, ultimately leading to fibrosis (51, 52), as well as with lung cancer, chronic obstructive pulmonary disease (COPD), pulmonary tuberculosis, and other pulmonary-associated diseases (1, 4). **Amorphous silica**, on the contrary, is generally considered to be less harmful, although exposure to this polymorph of silica is less studied (1). The comprehensive review of *Napierska et al.* (1) showed that the toxicological effect of SiNPs is associated with their physicochemical properties. These properties are the result of their synthesis method, and as a result, may cause different toxicological endpoints *in vitro* and *in vivo* (1, 4). ***In vitro* studies** usually describe the cyto-, geno-, immuno-, neurotoxicity effects, as well as the effects on blood cells and endothelial dysfunction of various SiNPs (4). Many studies show no adverse effects at lower concentrations, although at higher concentrations changes may occur (53-55). ***In vivo* studies** can be classified by duration and route of exposure. Acute exposure studies focus on the distribution of the SiNPs within the subjects, while chronic exposure studies aim to investigate

the long(er) term health effects. As mentioned previously, the main exposure routes can be divided into oral, transdermal, and parental routes (4). For every route, increased levels of SiNPs can be observed in the lung and liver (4, 56). SiNPs ingested orally may also lead to increased levels of SiNPs in the kidney and spleen (57, 58). This increased uptake is dependent on both the size and aspect ratio of the nanoparticles, as smaller particles are easier to be taken up by cells than larger ones (57). Most studies report no significant change in systemic toxicity (4, 56). However, there is still a lot of uncertainty surrounding the safety of SiNPs. Due to the number of studies being limited, the results of the *in vitro* and *in vivo* studies may contradict each other. The overall conclusion seems to be that SiNPs were taken up by the system and could induce an acute adverse effect, but no significant long-term systemic toxicity was observed. As the PMOs in this project are novel, we decided to include an **initial *in vitro* toxicity study**. A previous study by *Teng et al.* with similar triple-shell PMOs showed no significant change in the *in vitro* cell viability in human embryo kidney cells with an administered nanoparticle concentration up to 400 µg/ml (15). As the oral route is the most common exposure route, we will be studying the effect of PMOs in various concentrations on cell viability *in vitro* in Caco-2 cells. These epithelial cells are isolated from colon tissue and mimic a GI environment (59).

In summary, this project aims to optimize and characterize these novel hollow-core PMOs, as well as to assess their biosafety *in vitro* in comparison to conventional PMOs. The presence of the hollow core and the additional layers are expected to increase both the size and the loading capacity of the nanoparticles. Additionally, the PMOs are expected to be biocompatible and elicit no significant effect on cell viability *in vitro*.

EXPERIMENTAL PROCEDURES

Materials – Cetyltrimethylammonium bromide (CTAB), and Tetraethoxysilane (TEOS), were purchased from Sigma-Aldrich (St. Louis, MO, USA). Ethanol (EtOH, absolute and 96%), and concentrated ammonia aqueous solution (NH_{3(aq)}, 25 wt%) were purchased from VWR Chemicals (Radnor, PA, USA). Bis(triethoxysilyl)ethane (BTSE), Phosphate-Buffered Saline (PBS), Dulbecco's Phosphate-Buffered Saline (DPBS),

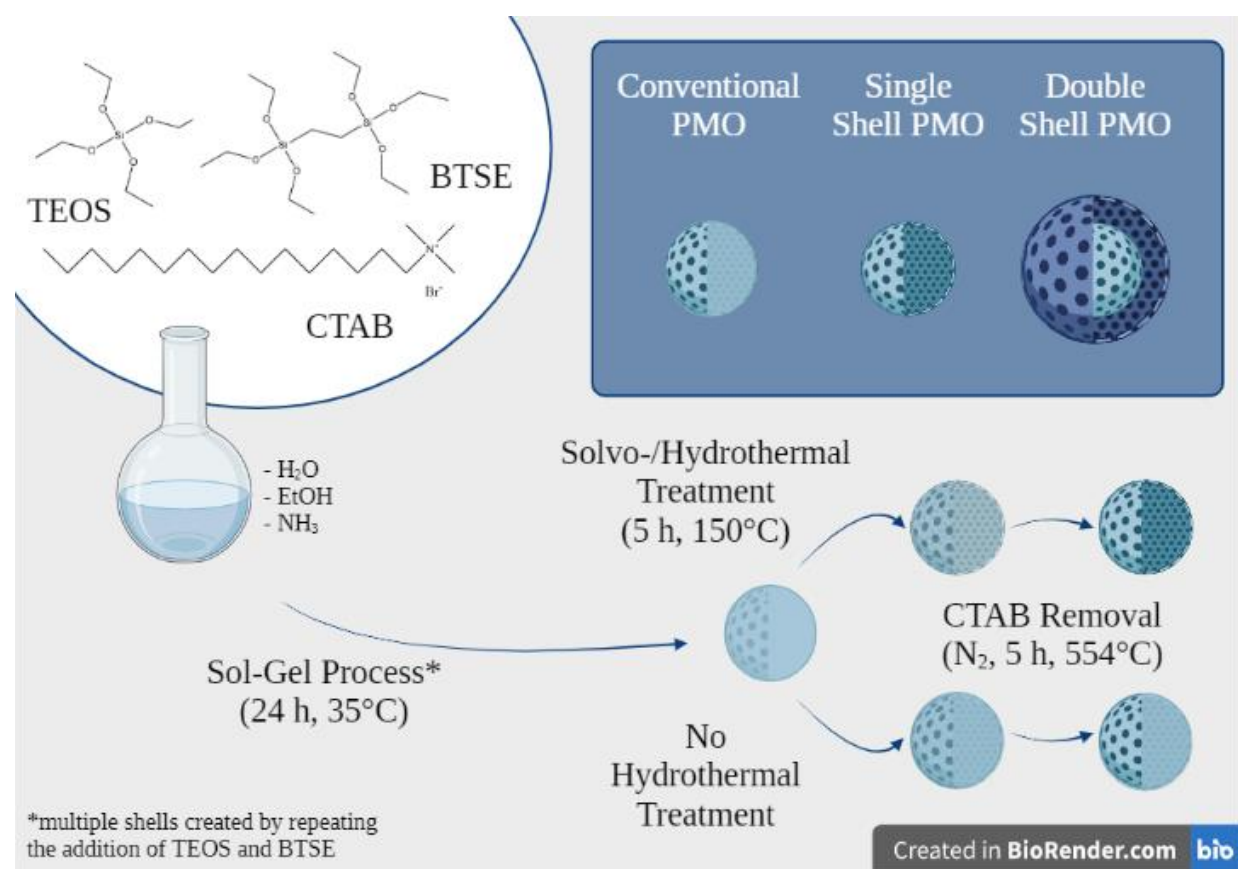


Fig. 1. Sol-gel synthesis of PMOs. Silica precursors (TEOS and BTSE) were added to a solution containing CTAB in water (H₂O), ethanol (EtOH), and ammonia (NH₃). After 24 hours, the product either underwent a hydrothermal treatment in water, a solvothermal treatment in ethanol, or was left as is. The CTAB templates were removed by calcination in N₂. Created with BioRender.com.

Dulbecco's Modified Eagle Medium (DMEM), Fetal Bovine Serum (FBS), CyQUANT™ Lactate Dehydrogenase (LDH) Cytotoxicity Assay Kit, and Invitrogen™ Image-IT Live Green Reactive oxygen species detection kit were purchased from Thermo Fisher Scientific (Waltham, MA, USA). MTT Cell Proliferation Assay (30-1010K) was purchased from ATCC (Manassas, VA, USA).

PMO Synthesis – PMOs were created using a sol-gel process guided by a surfactant template (Fig. 1). CTAB (0.16 g) was dissolved in a solution containing water (75 ml, Millipore), EtOH (30 ml, absolute) and NH_{3(aq)} (1.0 ml, 25 wt%). After stirring (1 h, 750 rpm, 35°C), varying amounts of TEOS and BTSE in a 1:1 volume ratio were added to the mixture, after which the mixture again was left to stir (24 h, 750 rpm, 35°C). Additional layers were created by repeating the addition of TEOS/BTSE, followed by an additional stirring

period (24 hours, 35°C). The product was collected via centrifugation (10 min, 10,000 rpm, 20°C), washed twice using EtOH (96%, 30 ml), and left to dry overnight. Next, the product was exposed to a solvothermal or hydrothermal treatment. The product was dispersed in EtOH (solvothermal, 60 ml) or H₂O (hydrothermal, 80 ml, Millipore), transferred to a Teflon-lined hydrothermal reactor, and subsequently heated (5 h, 150°C). To create conventional PMOs, this thermal treatment was skipped. Lastly, the product underwent calcination in N₂ with a heating rate of 10°C/min, followed by heating (5 h, 550°C) to remove the CTAB surfactant template. Samples will be referred to as followed: [C/S/H]_# of layers; with C indicating conventional PMOs, S indicating PMOs exposed to a solvothermal treatment, and H indicating PMOs exposed to a hydrothermal treatment.

Characterization – Transmission electron microscopy (TEM) images were obtained using a FEI Tecnai G2 Spirit Twin at 120 kV. Dry nanoparticle samples were ultrasonically suspended in ethanol and supported onto a carbon-coated copper grid. Images were analyzed using the Fiji (ImageJ[®]) software (60). **Nitrogen (N₂) sorption** isotherms were obtained using a Micromeritics TriStar II 3020 analyzer. Dry nanoparticle samples were degassed with N₂ gas (overnight, 150°C) before analysis. The specific surface area (S_{BET}) was estimated with the Brunauer-Emmett-Teller (BET) method and the total pore volume (V_{total}) was estimated with Barrett-Joyner-Halenda (BJH) analysis using data at a relative pressure (p/p⁰) of >0.99. The pore size distributions were calculated using the density functional theory (DFT). **Dynamic light scattering (DLS)** analysis was obtained by using a Brookhaven ZetaPALS analyzer and a Malvern Zetasizer Ultra to determine the hydrodynamic diameter and polydispersity index (PDI) of the nanoparticle samples. Dry nanoparticle samples were suspended in various media (1 mg/ml) and ultra-sonicated (30 min) before analysis. Each sample measurement was repeated 5 times and averaged. **The zeta potential** of the PMOs was measured using a Brookhaven ZetaPALS analyzer. Dry nanoparticle samples were suspended in water (Millipore, 1 mg/ml) and ultra-sonicated (5 min) before measuring. **Fourier transform infrared spectroscopy (FTIR)** spectra were collected on a Bruker Vertex 70, using KBr pellets of the solid sample.

In vitro Cytotoxicity – Caco-2 cells were seeded into 96-well culture plates at a density of 8,000 cells/well and incubated (4-5 days, 37°C, 5% CO₂) to obtain a monolayer. The culture medium was replaced with DMEM culture medium (FBS/phenol red⁻) for all assays. To obtain stock solutions, PMOs were suspended in filtered and autoclaved Millipore water. Stock solutions were further diluted in DMEM culture medium (FBS/phenol red⁻). PMOs were exposed to the cell culture (for 24 h, 37°C, 5% CO₂). For the **MTT assay** (MTT Cell Proliferation Assay, 30-1010K, ATCC, USA), MTT Reagent (10 µl) was added to the medium, and the culture was incubated again (37°C, 5% CO₂, in the dark) until the formazan product was visible (2-4 hours). Afterwards, Detergent Reagent (100 µl) was added to the

medium and was left to incubate (overnight, at room temperature, in the dark). For the **LDH assay** (Lactate Dehydrogenase (LDH) Cytotoxicity Assay Kit, CyQUANT[™], USA), a lysis buffer was added to several control wells 40 min before performing the assay to determine the maximum LDH release. After incubation, 50 µl of each sample medium was transferred to a clear 96-well plate, to which Reaction Mixture (50 µl) was added. The mixture was incubated (30 min, at room temperature, in the dark) before Stop Solution (50 µl) was added. For the **H₂DCFDA assay** (Image-IT Live Green Reactive oxygen species detection kit, Invitrogen[™], USA), carboxy-H₂DCFDA solution (25 µl) was added to the cell culture medium, after which the cells were left to incubate (40 min, 37°C, 5% CO₂). Next, the cells were washed twice with DPBS before measurement. All plates were measured using a FLUOstar Omega Microplate Reader. The absorbance of the MTT assay was read at 570 nm, the absorbance of the LDH assay was read at 490 nm, and the background at 680 nm. The fluorescence of the H₂DCFDA assay was read at an excitation and emission of 485 nm and 520 nm respectively. Technical replicates of the MTT assay were performed in duplicate, while technical replicates of the LDH and H₂DCFDA assays were performed in triplicate.

Statistical analysis – All data were statistically processed using the JMP[®] Pro 16.2.0 software (SAS Institute Inc., Cary, NC, 1989–2021). *In vitro* cytotoxicity results were analyzed using a Kruskal-Wallis *H* test with a *post hoc* Dunnett's test. Statistical significance was set at *p < 0.05.

RESULTS AND DISCUSSION

Effect of the precursor content on PMO morphology – PMOs were synthesized with a varying total precursor content in a 1:1 volume ratio and subsequently exposed to a solvothermal treatment. These PMOs will be denoted as S_[# layers]_total precursor content (µl)].

Transmission electron microscopy (TEM) images (Fig. 2) showed spherical structures. The average diameter of the single- (Fig. S1) and double- (Fig. S2) layer PMOs was determined based on a minimum of 100 PMOs. Single-layer PMOs with a total precursor content of 250 µl per layer (S_{1_250}) did not have a hollow core (Fig. 2b) and had an average size of 234 ± 17 nm. With an increasing number of layers, the size of the

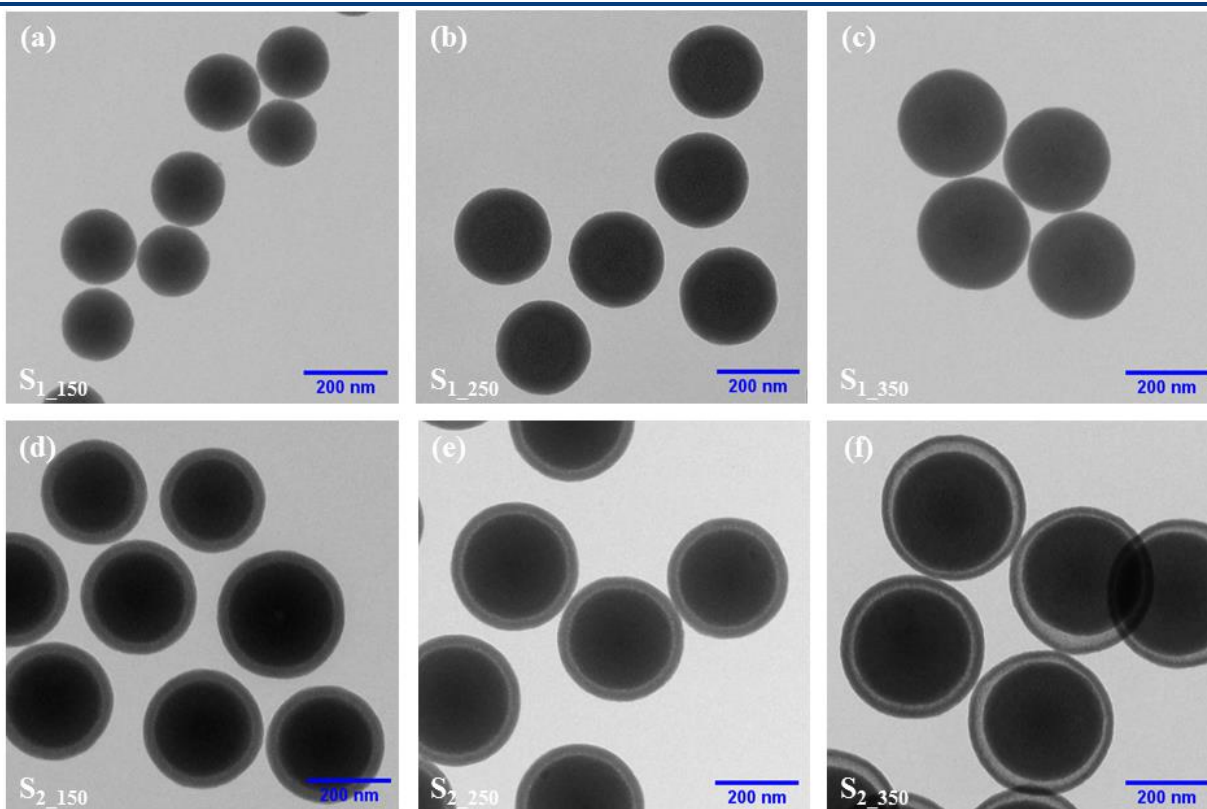


Fig. 2. Transmission electron microscopy (TEM) images of PMOs exposed to a solvothermal treatment. (a-c) Single-, and (d-f) double-layer PMOs were synthesized using the sol-gel method with exposure to a solvothermal treatment in ethanol. A total precursor content of 150 μl (left), 250 μl (middle), or 350 μl (right) per layer was used.

nanoparticles also increased to 291 ± 36 nm for $S_{2,250}$ PMOs. The inner layer of the double (Fig. 2e) layer PMOs with a similar precursor content per layer were again not hollow. This was the result of exposing the PMOs to a solvothermal treatment, instead of a hydrothermal treatment. Networks containing TEOS have a low condensation degree, and will easily dissolve when reacting with water, leading to small defects in the silica structure. These defects tend to form more within the middle parts of each nanoparticle layer. Meanwhile, the networks based on BTSE have a higher condensation degree and will act as a nucleation center for the dissolved organosilica composites, resulting in a separation of the nanoparticle into a core and a shell structure (15, 19). As there was no hydrothermal treatment of the PMOs, just a solvothermal treatment, this core and shell structure was not formed. As for why these defects formed in the core and not the outer layer, we hypothesized that due to the low condensation degree of TEOS,

this precursor will hydrolyze more quickly than BTSE. This subsequently results in more TEOS being present in the core than in the outer region. In future research, the addition time of the precursors can be changed, e.g. adding BTSE first, followed by TEOS after 30 minutes, to investigate this hypothesis. Changing the precursor content per layer influenced the size of the PMOs. An increase in precursor content was paired with an increase in size. At the lowest precursor content of 150 μl per layer ($S_{1,150}$, Fig. 2a), the PMOs had an average diameter of 177 ± 12 nm, whereas increasing the precursor content up to 250 μl ($S_{1,250}$, Fig. 2b) or 350 μl ($S_{1,350}$, Fig. 2c) per layer resulted in PMOs with a diameter of 234 ± 17 nm or 253 ± 34 nm respectively. Similarly, the diameter of double-layer PMOs increased from 279 ± 13 nm to 291 ± 36 nm and 351 ± 16 nm when increasing the total precursor content from 150 μl (Fig. 2d) to 250 μl (Fig. 2e) and 350 μl (Fig. 2f). This increase could be explained by the higher precursor content

added. As the precursors are added to the solution containing the CTAB micelles, they are hydrolyzed and condensed around the micelles to form the PMOs (15). As long as there are precursors present in the solution, this reaction can proceed, thus more precursors present will result in the reaction being able to go on longer, and consequently, a larger PMO will be formed. As the double-layer PMOs were not hollow, there was no inner shell of which the thickness could be determined. The thickness of the second layer slightly decreased with an increasing precursor content, changing from 25 ± 1 nm for $S_{2,150}$ PMOs to 22 ± 2 nm ($S_{2,250}$) and 22 ± 3 nm ($S_{2,350}$). As the precursor content increased, the thickness of the layer did not vary. The size of the initial layer however did vary depending on the precursor content, as mentioned previously. $S_{2,150}$ PMOs had an initial core size of 222 ± 14 nm, increasing up to 238 ± 32 nm and 290 ± 34 nm for $S_{2,250}$ and $S_{2,350}$ PMOs respectively. The resulting void space between the initial and second layer in the $S_{2,250}$ PMOs (Fig. 2e) was 5 ± 2 nm. Increasing the precursor content resulted in a larger void space of 9 ± 3 nm (Fig. 2f), whereas decreasing the precursor content resulted in almost no void space of 3 ± 1 nm (Fig. 2d). This could again be attributed to the change in precursor content. More precursors available will result in a larger initial layer (15). The void space may be influenced by the condensation degree of the precursor. We hypothesized that the TEOS network will hydrolyze and condensate quicker than the BTSE network, forming an initial layer around the first layer. Due to the exposure to water during the synthesis process, this TEOS would then again dissolve, creating a larger void if more TEOS is present (e.g. a higher precursor content). In future research, changing the precursor content of the second layer while keeping the precursor content of the initial layer the same could give further insight into the formation of the PMOs.

Nitrogen sorption isotherms indicated the formed PMOs were mesoporous. The isotherms (Fig. S3a,b) were of type IV, characterized by a hysteresis loop in the p/p^0 range between 0.4 and 1.0 according to the IUPAC recommendations (61). This hysteresis can be assigned to the capillary condensation of N_2 in the mesopores. The loops of PMOs with a lower precursor content per layer resembled an H4 hysteresis loop, indicating narrow, slit-like pores (61). On the contrary, PMOs with a

higher precursor content per layer or the presence of multiple layers had a defined H2 hysteresis loop, indicating the presence of 'ink bottle' shaped pores (61, 62). The beginning of the isotherm resembled a type II curve, which could be explained by the micropores present in the formed silica structure itself (61, 62). The specific surface area (S_{BET}) ranged between 919 and 1192 m^2/g , and between 946 and 1066 m^2/g for the PMOs with one or two layers respectively, varying by their initial precursor content (Table S1). There was no significant difference in S_{BET} values for all PMOs. The total pore volume (V_{Total}) ranged between 0.97 and 1.08 cm^3/g , and between 0.89 and 0.96 cm^3/g for the PMOs with one or two layers respectively, again varying by their initial precursor content (Table S1). With an increasing number of layers, the total pore volume slightly decreased. The pore size distributions (Fig. S3c,d) showed characteristic peaks within the 10 to 20 Å (1 to 2 nm) and the 20 to 50 Å (2 to 5 nm) ranges, indicating micropores and mesopores respectively. Interestingly, additional peaks around 60 Å (6 nm), 90 Å (9 nm), and 140 Å (14 nm) were observed in the distributions of the double-layer PMOs (Fig. S3d). Initially, these peaks were thought to be derived from the void space between the layers, however, these sizes did not match. As they were present in all samples exposed to a thermal treatment, we believed these pores were present in the silica network of the PMOs due to this exposure. This was further confirmed by the pore size distribution of untreated C_1 PMOs (Fig. 4b), as these peaks were not observed in this distribution. The void space between the layers could not be individually observed due to their small size, resulting in an overlap with the mesopores sizes in the silica network.

Dynamic light scattering (DLS) measurements showed an increased hydrodynamic diameter with an increasing number of layers. Additionally, the DLS measurements showed an increased hydrodynamic diameter with increasing precursor content. Single-layer PMOs diameters ranged from approximately 200 to 290 nm (Fig. S1) when the total precursor content was increased from 150 μl to 350 μl . Similarly, double layer PMO diameters ranged from 320 to 550 nm (Fig. S2). Larger hydrodynamic diameters present in the distribution of the $S_{2,350}$ PMOs (Fig. S2c) indicated agglomeration of the PMOs in

Table 1. Synthesis parameters of selected nanoparticles.

Nanoparticle	[TEOS+BTSE] _{total} per layer (μl)	Number of layers	Treatment
C ₁	250	1	No
S ₂	250	2	Solvothermal
H ₁	250	1	Hydrothermal
H ₂	250	2	Hydrothermal

TEOS: Tetraethoxysilane; BTSE: Bis(triethoxysilyl)ethane

water. The polydispersity index (PDI) of the samples was relatively low (< 0.05), indicating monodispersed samples (63). When observing the solutions for a week, sedimentation (Fig. S4) occurred at higher precursor content, as well as at an increase in layers. Both a higher precursor content and an increase in the number of layers increased the PMO size. Increasing the size resulted in heavier individual PMOs which were more prone to sediment.

Characterization of selected PMOs – Based on the previous morphologies, a total precursor content of 250 μl was selected for all further synthesis. PMOs with a lower precursor content did form no or very small void spaces between the additional layers, as visualized by TEM, which was expected due to exposure to a solvothermal treatment instead of a hydrothermal treatment. PMOs with a higher precursor content tended to agglomerate and sediment in water, evident from the DLS measurements. As for the pore size, S_{BET} and V_{total} results were similar for all precursor contents. Larger batches of the PMOs could be synthesized by upscaling the synthesis. PMOs were exposed to a hydrothermal treatment during the synthesis, instead of a solvothermal treatment, resulting in a transformation of each layer into a hollow shell variant. C₁ PMOs were synthesized without any additional treatment as a reference. S₂ PMOs were included as a non-hollow core comparison for the double-shell hollow-core

PMOs. An overview of the different PMOs synthesized is given in Table 1.

TEM images showed spherical nanoparticles. C₁ PMOs (Fig. 3a) had a diameter of 202 ± 10 nm. S₂ PMOs (Fig. 3d) again did not have a hollow core. They were larger with a diameter of 272 ± 39 nm and an initial layer size of 222 ± 36 nm. The thickness of the second layer was 21 ± 3 nm, with a void space of 5 ± 2 nm. These results were similar to the previously described results. Likewise, this indicated the successful scalability of the synthesis. PMOs exposed to a hydrothermal treatment with one (Fig. 3b) or two (Fig. 3e) shells did have a hollow core structure. H₁ PMOs had a diameter of 245 ± 13 nm, while H₂ PMOs were larger with a diameter of 332 ± 13 nm and an initial shell size of 271 ± 12 nm. H₁ PMOs had a shell thickness of 35 ± 6 nm. H₂ PMOs had a slightly thicker initial shell of 41 ± 5 nm, however, the second shell was thinner, with a thickness of 14 ± 2 nm. The void space between both shells was 17 ± 2 nm. Interestingly, the size of the hollow cores of these PMOs increased from 175 ± 15 nm (H₁) to 189 ± 14 nm (H₂), whereas the hollow-core size of another batch of unreported PMOs decreased from 189 ± 16 nm to 177 ± 19 nm with the addition of a second shell. The PMOs of the other batch had an initial shell size of 255 ± 18 nm and 265 ± 15 nm respectively. An increase in size of the initial shell was thus paired with a larger inner hollow-core size. PMOs with exposure to a hydrothermal treatment were notably larger. This was attributed

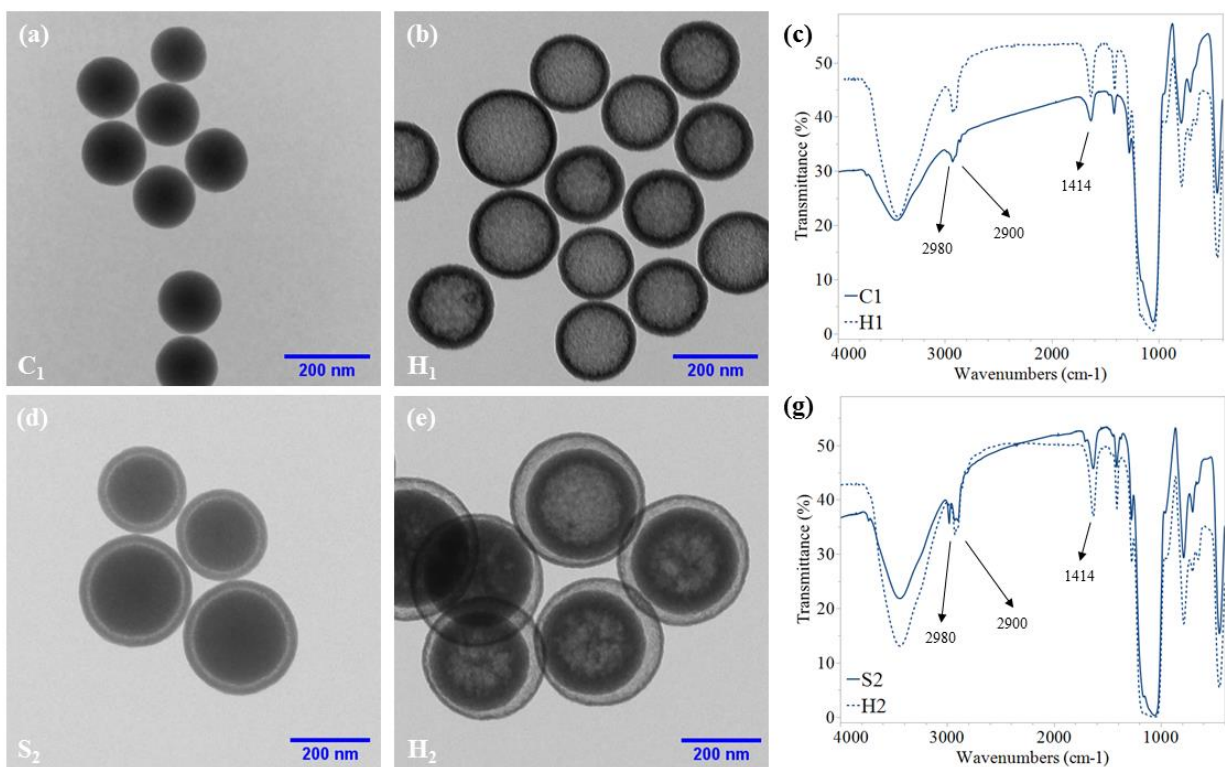


Fig. 3. Transmission electron microscopy (TEM) images and Fourier transform infra-red (FTIR) spectra of selected nanoparticles. (a) TEM image of C₁ PMOs. (b) TEM image of H₁ PMOs. (c) FTIR spectra of single-layer nanoparticles (C₁ and H₁ PMOs). (d) TEM image of S₂ PMOs. (e) TEM image of H₂ PMOs. (f) FTIR spectra of double-layer nanoparticles (S₂ and H₂ PMOs).

to the exposure to the hydrothermal treatment. As mentioned previously, networks containing TEOS have a lower condensation degree than those containing BTSE and will dissolve when exposed to a hydrothermal treatment, resulting in small defects in the silica network. The dissolved organosilica composites then react with the nucleation centers, forming the shell structure (15, 19). This further explained the thinner outer shell, as well as the larger void space when comparing the double-shell PMOs, as the TEOS composites between both shells will react with both the inner and outer shell. The thickness of the shells can be further adjusted by adjusting the temperature of the reaction. A lower temperature will result in a smaller shell, whereas a higher temperature will lead to a thicker shell (15).

Fourier transform infra-red (FTIR) spectra of the PMOs (Fig. 3c, f) showed peaks in the functional groups' region around 2900 cm⁻¹ and 2980 cm⁻¹. These peaks are characteristic of the

stretch vibrations between the alkane bonds (C – H) within the silica network itself. It could be argued these peaks were derived from the CTAB template not being fully removed by the calcination, contaminating the sample. However, CTAB would show an additional peak around 1470 cm⁻¹, which was absent in these samples (64). Additionally, our FTIR spectra matched the spectra of similar PMOs, in which solvent extraction was used to remove the CTAB template (15). This confirmed the successful removal of CTAB by calcination. Next, a broad C – O stretching band between 1000 cm⁻¹ and 1350 cm⁻¹ could be observed, indicating the presence of hydroxyl groups. This was further confirmed by a broad O – H stretch between 3200 cm⁻¹ and 3590 cm⁻¹. Lastly, the peak in the fingerprint region at 1414 cm⁻¹ could be assigned to the bending vibration of the C – H bond.

Nitrogen sorption isotherms indicated the formed PMOs were mesoporous (Fig. 4a). The isotherms were again of type IV with a

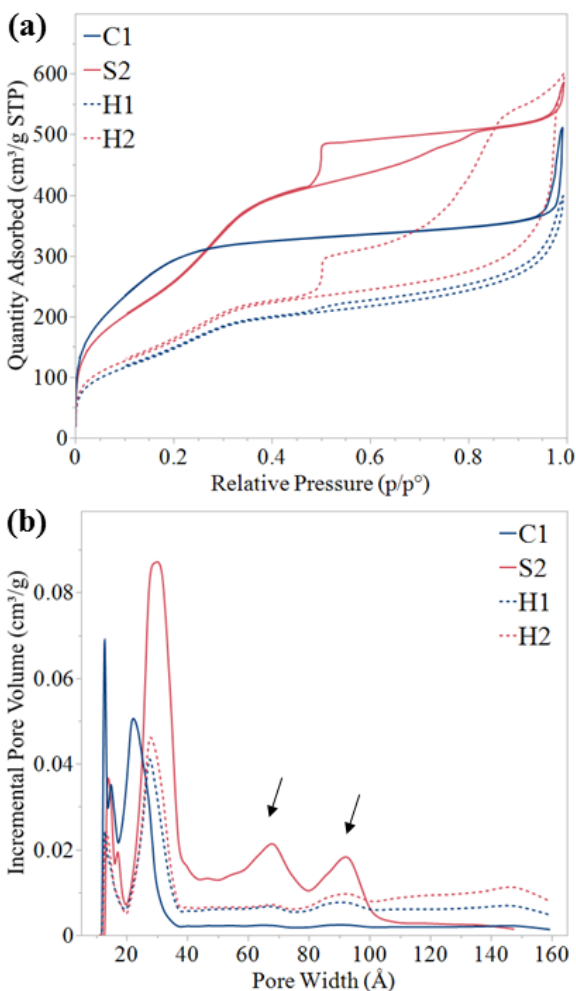


Fig. 4. Nitrogen sorption analysis of the selected nanoparticles. **(a)** Nitrogen sorption isotherms. **(b)** Pore size distributions.

characteristic hysteresis loop in the p/p^0 range between 0.5 and 1.0 (61). Whereas C_1 PMOs had a hysteresis loop resembling an H1 loop, indicating narrow, uniform mesopores, H_1 PMOs had an H4 loop, indicating narrow, slit-like pores (61). Loops of both double-layer PMOs resembled an H2 hysteresis loop, indicating ink-bottle-shaped pores (61, 62). Additionally, the start of the isotherm again resembled a type II isotherm, indicating the micropores in the silica layers themselves. The specific surface area (S_{BET}) of the PMOs was $1090 \text{ m}^2/\text{g}$ (C_1), $1015 \text{ m}^2/\text{g}$ (S_2), $517 \text{ m}^2/\text{g}$ (H_1), and $617 \text{ m}^2/\text{g}$ (H_2) (Table S3). S_2 PMOs had a similar specific surface area as previously described. Hollow-core PMOs were shown to have a lower specific surface area than both C_1 and S_2 PMOs.

This specific surface area was also lower than reported for comparable PMOs, as an S_{BET} of up to $975 \text{ m}^2/\text{g}$ for hollow single-shell PMOs was reported (19). The total pore volume (V_{Total}) was $0.79 \text{ cm}^3/\text{g}$ (C_1), $0.91 \text{ cm}^3/\text{g}$ (S_2), $0.62 \text{ cm}^3/\text{g}$ (H_1), and $0.92 \text{ cm}^3/\text{g}$ (H_2) (Table S3). S_2 PMOs again were comparable to the previously described PMOs. Pore size distributions (Fig. 4b) again showed characteristic peaks between 10 \AA and 20 \AA and between 20 \AA and 50 \AA , indicating micropores and mesopores respectively. However, a notable shift of the mesopores peak was observed when comparing conventional PMOs (C_1) to all other samples. We hypothesized this shift was the result of exposing the PMOs to a thermal treatment, consequently slightly changing the structure of the silica network, forming larger pores. Additional peaks around 60 \AA (6 nm) and 90 \AA (9 nm) were present. As mentioned previously, we assumed these peaks to belong to pores formed due to the thermal treatment. This suspicion was further enhanced by the change in isotherm hysteresis, as there was a notable change in pore shape.

DLS measurements of the PMOs in water (Table S2) showed a hydrodynamic diameter of $260 \pm 3 \text{ nm}$ (C_1), $304 \pm 31 \text{ nm}$ (S_2), $350 \pm 15 \text{ nm}$ (H_1), and $478 \pm 5 \text{ nm}$ (H_2). The polydispersity index (PDI) of these samples was relatively low (< 0.2), indicating monodispersed samples (63). As the number of layers increased, the hydrodynamic diameter also increased. Hollow-core PMOs were again larger than nanoparticles without a hollow core. These results were in line with the TEM analysis of the PMOs. Hydrodynamic diameters were larger than the actual diameter determined by TEM analysis, due to the interaction of the PMOs with the aqueous environment. Additionally, hollow-core PMOs showed some agglomeration, which was accompanied by a slightly higher PDI, in comparison to PMOs without a hollow core. When exposed to other media than water, the hydrodynamic diameter of the PMOs changed due to the presence of other ions or proteins in the liquid. PBS is a commonly used buffer in biomedical research as the ion concentrations mimic those in the human body. In addition to water, it commonly contains ions derived from NaCl, KCl, Na_2HPO_4 , and KH_2PO_4 (65, 66). DMEM cell culture medium contains vitamins, amino acids, and glucose among other things, which aid the growth of cells (66, 67). FBS is

commonly added to the cell culture medium to further improve cell proliferation. It contains additional growth factors, hormones, lipids, transport proteins, etc. (67). All these ions and proteins may interact with the PMOs, resulting in a protein corona surrounding the PMO, increasing its size and consequently its interactions with the environment and other PMOs. Dispersing the PMOs in PBS resulted in increased agglomeration by all PMOs (Fig. S6). The hydrodynamic diameter of an individual PMO also increased up to approximately 450 nm for H₁, H₂, and S₂ PMOs. C₁ PMOs had an even larger hydrodynamic diameter of 750 nm. The introduction of proteins in DMEM cell culture medium resulted again in agglomeration of the PMOs, although slightly less than when the PMOs were exposed to just PBS. The hydrodynamic diameters of the individual PMOs stayed relatively similar to when they dispersed in PBS. C₁ PMOs had a hydrodynamic diameter of 280 nm, whereas H₁ PMOs had a hydrodynamic diameter of 440 nm. Interestingly, both double-layer PMOs had a hydrodynamic diameter of 450 nm. The addition of FBS to the culture medium resulted in even less agglomeration of the PMOs compared to PBS or purely DMEM. Individual hydrodynamic diameters were similar to the double-layer PMOs, averaging at 450 nm. For single-layer PMOs, the hydrodynamic diameter was reduced to 240 nm (C₁) and 350 nm (H₁) compared to the culture medium without FBS. As mentioned previously, biological media contain many different ions and proteins. In water, the PMO surface will be negatively charged due to the dissociation of the silanols, resulting in electrostatic repulsion between the particles, and consequently, agglomeration is less likely to occur. The ions and proteins present in biological media will interact with the surface, forming a protein corona, which in turn reduces these electrostatic forces, resulting in increased agglomeration of the PMOs. Besides the presence of ions and protein, the pH of the solution may also play a part in agglomeration (71, 72). At a low pH, silica nanoparticles are relatively stable, however, they tend to coagulate at a higher pH (66). As most biological media have a pH of around 7.4, the observed agglomeration was expected. For the media enriched with FBS, reported results are conflicting. Some studies report C₁ remaining stable (68, 69), whereas others showed agglomeration (69, 70), depending on their surface

functionalization. When the PMO solutions were measured after 24 hours (Fig. S6), most solutions showed similar amounts of agglomeration as the previous day. However, in PBS, more agglomeration could be observed for all PMOs, indicated by a shift of the distribution to larger sizes. Interestingly, after 24 hours, peaks at very small sizes could be observed. These peaks were thought to be due to the degradation of the silica network. This process generally occurs at a higher pH. It has been shown that exposing silica nanoparticles to a wide variety of media can result in degradation (66, 71). In water, the nanoparticle surfaces are attacked by hydroxyl groups, converting the siloxane groups into silanols groups. As a result, silicic acid is released, resulting in a slow degradation of the surface (72). This degradation is further enhanced when additional ions are present in the medium, as is the case with PBS, since these ions can adsorb onto the surface and weaken the siloxane bonds or enhance silanol deprotonation (66). It has been reported that in PBS, MSNs with a diameter of 200 nm showed full degradation within 6 hours (73). Larger (1,500 nm) and smaller (80 nm) MSNs showed similar results (73). For cell culture medium enriched with FBS, the results again vary. A study by *Hao et al.* showed no degradation in the absence of FBS, while the presence of FBS showed partial degradation (74).

Zeta potential measurements (Fig. 5) of the PMOs in water showed the PMOs were negatively charged, with zeta potentials of -23 ± 1 mV (C₁), -27 ± 4 mV (S₂), -32 ± 2 mV (H₁), and -30 ± 1 mV (H₂). Absolute zeta potential values of hollow-core PMOs were larger than those of their filled counterpart when initially brought into a solution. Large zeta potentials, either negative or positive, indicated a rather high degree of electrostatic interactions between the PMOs, leading to repulsion (75). The PMOs were not likely to form large agglomerates, as indicated by the hydrodynamic diameters and PDI obtained via DLS measurements. It should however be noted that the pH of the initial solution changed based on the type of PMO added to it. C₁ PMO solutions had a pH of 5.8, while H₁ PMO solutions had a pH of 5.2 and were slightly more acidic. Double-layer PMOs both had a pH of 6.3. As the size of a nanoparticle increased, although the total surface area increased, the surface-to-volume area decreased. Additionally, as single-layer PMOs were smaller

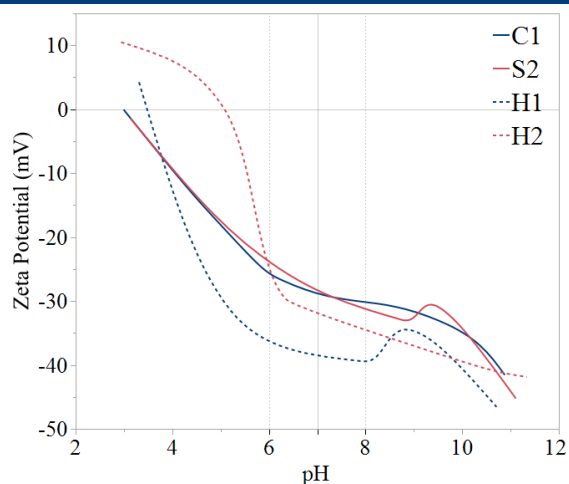


Fig. 5. Zeta potential (mV) in function of the pH of the selected PMOs.

than double-layer PMOs, they were lighter than their double-layer counterparts. A solution with the same concentration (e.g. 1 mg/ml), did contain more PMOs if they were smaller and/or lighter. More PMOs present in the solution, combined with an increased particle surface area containing more silanol groups, lead to a slightly more acidic environment of the sample. A similar result has been observed in other metal oxides, including titanium dioxide (TiO₂) (76). The pH was adjusted using HCl and NaOH solutions. At a low pH, which mimics the gastric environment a PMO would cross when being used as an oral drug delivery system, all PMOs were unstable, with zeta potentials between 0 and +10 mV. At a pH of 7.2-7.4, which equals the pH of the intestinal environment, the PMOs were relatively stable with zeta potential around -30 mV. Both C₁ and H₁ PMOs again had an absolute zeta potential value slightly larger than the double-layer PMOs. Similarly, hollow-core PMOs had an absolute zeta potential value larger than PMOs without a hollow core. Furthermore, by adjusting the pH, the isoelectric point (IEP) of each sample could be determined. This point indicates the pH at which the samples have a zeta potential of zero. For the selected PMOs (Table S2), this point was 3.0 (C₁), 3.0 (S₂), 3.5 (H₁), and 5.1 (H₂). Silica nanoparticles generally have an IEP at a pH lower than 2, although varying pHs between 1 and 4 have been reported (66, 77). An increase in the number of layers showed an increase in IEP. IEPs of hollow-core PMOs were also higher than those of

PMOs without a hollow core. The higher IEP of the hollow-core PMOs possibly explains their agglomeration observed in the DLS measurements. It has been shown before that, if the IEP of other nanoparticles (e.g. TiO₂) was close to the pH of the medium, agglomeration tends to occur (78). As the zeta potential at this point was zero, electrostatic repulsion between the particles no longer occurred, resulting in agglomeration. A slight change in solution pH consequently changed the zeta potential of the PMOs, and as a result, their interactions with their environment and other nanoparticles.

In summary, PMOs with(out) a hollow core and with multiple layers were successfully created. The presence of a hollow core, as well as an increased number of layers, increased the PMO size, as evident from TEM and DLS analysis. Nitrogen sorption showed that hollow-core PMOs had a smaller S_{BET} and V_{total} compared to PMOs without a hollow core. Lastly, hollow-core PMOs were more stable than PMOs without a hollow core when initially brought into a solution, but quickly became less stable, and were more likely to agglomerate as demonstrated by DLS measurements paired with zeta potential measurements.

In vitro Toxicity Study – To study the *in vitro* toxicological effect of the PMOs, a pilot study was included, in which Caco-2 cells were seeded and incubated with various concentrations of the PMOs for 24 h. After incubation, various assays were performed, including an MTT, an H₂DCFDA, and an LDH assay. Using the **MTT assay**, the relative metabolic activity of the cells could be determined, as the metabolic enzymes of living cells reduce the 3-(4,5-dimethylthiazol-2-yl)-2,5-diphenyltetrazolium bromide (MTT) to formazan. Living cells will contribute to higher metabolic activity than dead cells, thus the MTT assay indirectly provides information about the cell viability. For this assay, the cells were incubated with PMOs at concentrations between 10 and 500 µg/ml (Fig. 6a). As the sample size was small (n = 2), definitive conclusions should be formulated with caution. At lower PMO concentrations (10-250 µg/ml), no significant change in metabolic activity compared to the control was reported, although a slight increase could be observed. However, at a higher PMO

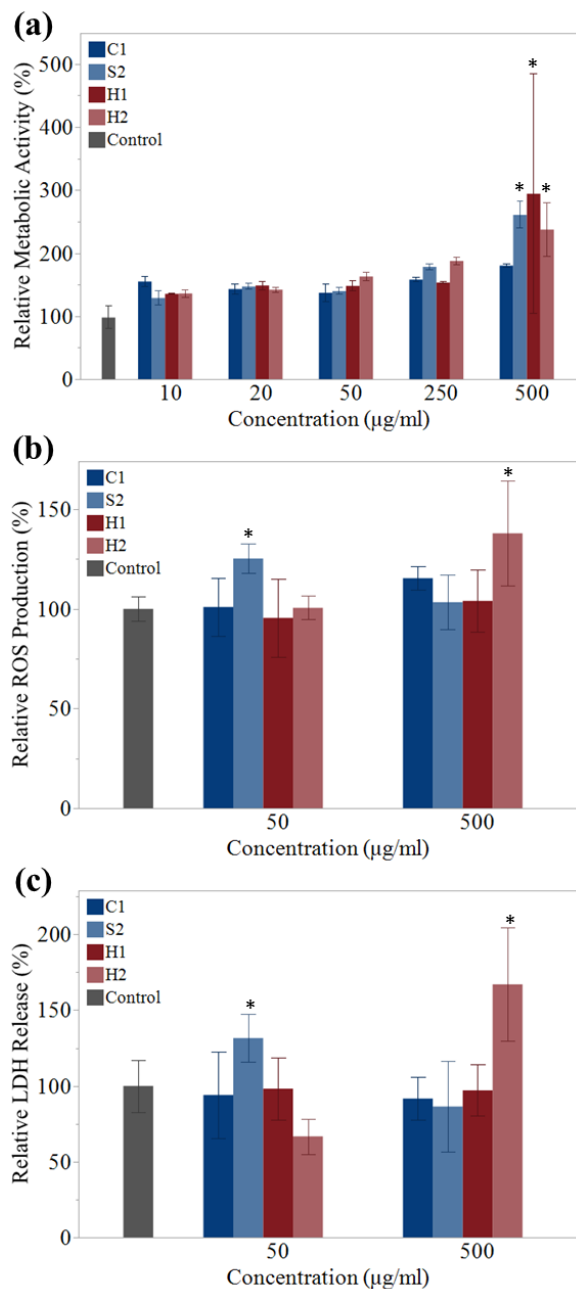


Fig. 6. *In vitro* cytotoxicity of Caco-2 cells incubated with various types of PMOs. Non-exposed controls were represented by the gray bar on the left. **(a)** Relative metabolic activity (%) of Caco-2 cells was determined by an MTT assay. $n = 2$. **(b)** Relative ROS production (%) of Caco-2 cells was determined by an H₂DCFDA assay. $n = 3$. **(c)** Relative LDH release (%) by Caco-2 cells was determined by an LDH assay. $n = 3$. All results were represented as mean \pm SD. * $p < 0.05$ compared to the control.

concentration (500 µg/ml), an increase in metabolic activity compared to the control could be observed for both S₂ and H₂ PMOs. Although exposure to H₁ PMOs resulted in increased metabolic activity as well, due to a high standard deviation, this increase could present itself due to an external factor and not solely due to the PMO exposure. In the **H₂DCFDA assay**, 2',7'-dichlorodihydrofluorescein diacetate (H₂DCFDA) was taken up by living cells, where it was deacetylated by cellular esterases and subsequently oxidized by reactive oxygen species (ROS) to 2',7'-dichlorofluorescein (DCF). The total amount of DCF oxidized can be used to determine ROS production. The cells were exposed to either a low (50 µg/ml) or high (500 µg/ml) concentration of PMOs (Fig. 6b). Exposure to a high concentration of H₂ PMOs resulted in an increased ROS production by the cells. A slight increase in ROS production could be observed when the cells were exposed to a low concentration of S₂ PMOs, however, at a higher concentration, this increase was no longer observed. Again, these results should be looked at with caution due to the small sample size ($n = 3$). Lastly, in the **LDH assay**, lactate dehydrogenase (LDH) released in the cell medium by cells with a damaged plasma membrane converts lactate to pyruvate by reducing NAD⁺ to NADH. This NADH is then used by diaphorase to reduce a tetrazolium salt (INT) to formazan. The cells were again exposed to either a low (50 µg/ml) or high (500 µg/ml) concentration of PMOs (Fig. 6c). Exposure to both a high concentration of H₂ PMOs and a low concentration of S₂ PMOs resulted in an increased LDH release compared to the non-exposed control. All other concentrations resulted in a slightly reduced LDH release, indicating no damage to the cell membrane, and subsequently, more living cells.

Based on these initial findings, C₁ and H₁ PMOs did not alter the cell viability significantly, which is a first step towards biocompatibility, but further testing is still necessary due to the small sample size, the absence of biological replications, and other parameters including genotoxicity, immunogenicity, mutagenicity, and carcinogenicity (4). Exposure to high concentrations of S₂ or H₂ PMOs indicated an enhanced cell growth. These results were unexpected, as the MTT assay, although a commonly used cell viability assay, is known to overestimate the cytotoxicity of MSNs (79). Consequently, slightly reduced (79, 80) or

unchanged (15, 81) levels of metabolic activity were expected at lower concentrations, as concentrations as high as 500 µg/ml have not been reported yet. A common byproduct of these metabolic reactions in cells is ROS. These chemicals play a role in cell signaling, but can also be harmful to the cell if a surplus is present in the cell due to increased production or failed elimination, leading to oxidative stress (82). Many studies describe the induction of ROS when cells were exposed to various types of silica nanoparticles (55, 83). Additionally, exposure of cells to silica nanoparticles specifically formed by a Stöber synthesis was correlated with the induction of oxidative stress within these cells (54). However, it is not fully clear yet how the silica nanoparticles induce ROS (55). At exposure to a low concentration of S₂ PMOs or a high concentration of H₂ PMOs, increased ROS levels could be observed. This could just be the result of the increased metabolic activity, with no major cytotoxic consequences for the cell. Therefore, we decided on including an LDH assay to assess membrane damage, and subsequently, cytotoxicity. A large amount of ROS present in cells is known to induce apoptosis, resulting in cell death and consequently increased levels of LDH. Similar to the H₂DCFDA assay results, exposure to a low concentration of S₂ PMOs or a high concentration of H₂ PMOs lead to increased levels of LDH release. This release was assigned to reduced membrane integrity of the cells, indicating a decrease in cell viability (81). A study by *Alkhamash et al.* suggested that larger silica nanoparticles adhered to vesicular lipid bilayers, resulting in membrane rupture, whereas smaller nanoparticles got engulfed by the vesicle (84). However, this membrane damage did not have to be the direct consequence of the elevated ROS levels. Cytotoxicity without the presence of oxidative stress has been reported before, with a possible mechanism being the disturbance of membrane integrity, although this effect is still poorly understood (81, 85). *Gehrke et al.* speculated that the disturbance of the membrane integrity was due to the silica nanoparticles interfering with the structural integrity of the membrane proteins (81).

Other factors influencing these results were the different morphologies of the PMOs, as well as their interactions with their environment. Our PMOs, as synthesized, had a diameter between

200 nm and 350 nm determined by TEM analysis (Fig. S5), increasing up to 500 nm in size when exposed to a liquid environment (e.g. water or DMEM cell culture medium), as evident from the DLS analysis (Fig. S6). Before being taken up by the cells, nanoparticles first have to sediment. This sedimentation is dependent on many factors, including size, density, and shape (86, 87). While all PMOs were of a similar spherical shape, S₂ and H₂ PMOs were notably larger than C₁ and H₁ PMOs, while also showing more agglomeration when exposed to cell culture media (Fig. S6). This size difference could lead to increased gravitational sedimentation of the particles, resulting in an uneven exposure of the cells on the surface (86). After exposure, the nanoparticles can be taken up passively or actively by cells via many routes (88). Silica nanoparticles are generally internalized by endocytosis, more specifically via the clathrin-mediated endocytotic pathway (88, 89). However, the optimal size for uptake via this pathway lies within the 120-150 nm range (88). The PMOs may thus be internalized by the cells using various routes depending on their size, leading to a variation in the number of PMOs taken up.

In summary, while this study only included an initial toxicological study with limited testing, the following trends could be observed based on these results. Exposure to single-layer PMOs could be regarded as biocompatible, however, exposure to double-layer PMOs resulted in at least some cellular agitation, indicated by increased metabolic activity, ROS production, and LDH release.

Future outlooks – Based on the previously discussed results, many outlooks for further research arise. Synthesis-wise, it could be interesting to look at the formation of the core and shell structure by taking samples during the synthesis and hydrothermal treatment at various points in time. This is however very labor-intensive and time-consuming. Next, adjusting the synthesis to create smaller double-layer PMOs could give us an idea of whether the observed cytotoxicity is indeed size-dependent. Lastly, the degradation of the PMOs is worth looking into. As evident from the DLS measurements, degradation may occur within 24 hours. It is uncertain if this degradation is due to the breakdown of the silica network, resulting in organosilica composites, or the degradation of the network, resulting in silicic acid.

This leads to another question, namely, are the trends noticeable in the *in vitro* study solely the result of PMO exposure, or are there other influences present? Depending on these results, additional functionalization could be introduced to the nanoparticle surface to increase stability and biocompatibility.

CONCLUSION

The use of nanomaterials in biomedical research is increasing quickly over the last few years. In our project, we set out to optimize PMOs as a novel and improved drug delivery system. Our PMOs showed no major differences in stability compared to conventional PMOs, however, a problem arising in all nanoparticle solutions was the agglomeration in biological media. Exposure to single-shell hollow-core PMOs did not alter cell viability significantly, indicating their biocompatibility, whereas exposure to multi-shell PMOs did result in some cellular agitation. Although further studies on stability, functionalization, and loading are definitely needed, these PMOs are shown to be promising candidates as a drug delivery system due to their easy and tunable synthesis, large mesoporous volume for drug loading, and biocompatibility. As a follow-up study, we propose studying the degradation of the PMOs, as well as creating smaller multi-shell PMOs to determine if the reported toxicological outcomes are indeed size-dependent.

Acknowledgements – We would like to thank Prof. Dr. Anitha Ethirajan for providing insight regarding the interaction between the PMOs and the biological media. Additionally, we are grateful to Dr. Ir. Bjorn Joos for performing the nitrogen sorption analysis and Mr. Dries De Sloovere for performing the FTIR analysis, as well as Ms. Birte Luyck for providing an introduction to using the DLS, and Ms. Buse Turkeli for providing insight into cell culture experiments.

Author contributions – CS, UV, NS, and AH conceived and designed the research. CS performed the experiments and the data analysis. UV assisted with the synthesis and characterization. NS assisted with the *in vitro* cytotoxicity study. CS wrote the paper.

REFERENCES

1. Napierska D, Thomassen LCJ, Lison D, Martens JA, Hoet PH. The nanosilica hazard: another variable entity. Part Fibre Toxicol. 2010;7(1):39-.
2. Gonçalves MC. Sol-gel Silica Nanoparticles in Medicine: A Natural Choice. Design, Synthesis and Products. Molecules. 2018;23(8):2021.
3. Rastegari E, Hsiao Y-J, Lai W-Y, Lai Y-H, Yang T-C, Chen S-J, et al. An Update on Mesoporous Silica Nanoparticle Applications in Nanomedicine. Pharmaceutics. 2021;13(7):1067.
4. Murugadoss S, Lison D, Godderis L, Van Den Brule S, Mast J, Brassinne F, et al. Toxicology of silica nanoparticles: an update. Arch Toxicol. 2017;91(9):2967-3010.
5. Rahman IA, Padavettan V. Synthesis of Silica Nanoparticles by Sol-Gel: Size-Dependent Properties, Surface Modification, and Applications in Silica-Polymer Nanocomposites—A Review. Journal of Nanomaterials. 2012;2012:132424.
6. Narayan R, Nayak UY, Raichur AM, Garg S. Mesoporous Silica Nanoparticles: A Comprehensive Review on Synthesis and Recent Advances. Pharmaceutics. 2018;10(3):118.
7. M Ways TM, Ng KW, Lau WM, Khutoryanskiy VV. Silica Nanoparticles in Transmucosal Drug Delivery. Pharmaceutics. 2020;12(8):751.
8. Beck JS, Vartuli JC, Roth WJ, Leonowicz ME, Kresge CT, Schmitt KD, et al. A new family of mesoporous molecular sieves prepared with liquid crystal templates. Journal of the American Chemical Society. 1992;114(27):10834-43.
9. Kresge CT, Leonowicz ME, Roth WJ, Vartuli JC, Beck JS. Ordered mesoporous molecular sieves synthesized by a liquid-crystal template mechanism. Nature. 1992;359(6397):710-2.
10. Yuan D, Ellis CM, Davis JJ. Mesoporous Silica Nanoparticles in Bioimaging. Materials (Basel). 2020;13(17):3795.
11. Zhou Y, Quan G, Wu Q, Zhang X, Niu B, Wu B, et al. Mesoporous silica nanoparticles for drug and gene delivery. Acta Pharm Sin B. 2018;8(2):165-77.
12. Park SS, Santha Moorthy M, Ha C-S. Periodic mesoporous organosilicas for advanced applications. NPG Asia Materials. 2014;6(4):e96-e.
13. Croissant JG, Cattoën X, Wong Chi Man M, Durand J-O, Khashab NM. Syntheses and applications of periodic mesoporous organosilica nanoparticles. Nanoscale. 2015;7(48):20318-34.
14. Poscher V, Salinas Y. Trends in Degradable Mesoporous Organosilica-Based Nanomaterials for Controlling Drug Delivery: A Mini Review. Materials. 2020;13:3668.
15. Teng Z, Su X, Zheng Y, Zhang J, Liu Y, Wang S, et al. A Facile Multi-interface Transformation Approach to Monodisperse Multiple-Shelled Periodic Mesoporous Organosilica Hollow Spheres. Journal of the American Chemical Society. 2015;137(24):7935-44.
16. Jiang M, Li S, Shi X, Gao T, Liu Z, Zhou G. Controllable morphology transition from vesicular to worm-like to vesicular multilamellar mesoporous silica induced by β -cyclodextrin. RSC Advances. 2016;6(80):76824-8.

17. Zhang Y, Zhou G, Sun B, Zhao M, Zhang J, Chen F. A cationic-cationic co-surfactant templating route for synthesizing well-defined multilamellar vesicular silica with an adjustable number of layers. *Chemical communications* (Cambridge, England). 2014;50.
18. Stöber W, Fink A, Bohn E. Controlled growth of monodisperse silica spheres in the micron size range. *Journal of Colloid and Interface Science*. 1968;26(1):62-9.
19. Teng Z, Wang S, Su X, Chen G, Liu Y, Luo Z, et al. Facile Synthesis of Yolk-Shell Structured Inorganic-Organic Hybrid Spheres with Ordered Radial Mesochannels. *Advanced Materials*. 2014;26(22):3741-7.
20. Liberman A, Mendez N, Trogler WC, Kummel AC. Synthesis and surface functionalization of silica nanoparticles for nanomedicine. *Surface Science Reports*. 2014;69(2):132-58.
21. Bharti C, Nagaich U, Pal AK, Gulati N. Mesoporous silica nanoparticles in target drug delivery system: A review. *Int J Pharm Investig*. 2015;5(3):124-33.
22. Qiao SZ, Lin CX, Jin Y, Li Z, Yan Z, Hao Z, et al. Surface-Functionalized Periodic Mesoporous Organosilica Hollow Spheres. *The Journal of Physical Chemistry C*. 2009;113(20):8673-82.
23. Trewyn BG, Slowing II, Giri S, Chen H-T, Lin VSY. Synthesis and Functionalization of a Mesoporous Silica Nanoparticle Based on the Sol-Gel Process and Applications in Controlled Release. *Accounts of Chemical Research*. 2007;40(9):846-53.
24. Kristl M, Ban I, Gyergyek S, Maver U, Stergar J. Sol-gel preparation of Ni_xCu_{1-x}/silica nanocomposites using different silica precursors. *Journal of Sol-Gel Science and Technology*. 2020.
25. Rong S, Chen S, Su P, Tang H, Jia M, Xia Y, et al. Postsynthetic Modification of Metal-Organic Frameworks by Vapor-Phase Grafting. *Inorganic Chemistry*. 2021;60(16):11745-9.
26. Qi J, Lai X, Wang J, Tang H, Ren H, Yang Y, et al. Multi-shelled hollow micro-/nanostructures. *Chemical Society Reviews*. 2015;44(19):6749-73.
27. Dong Z, Lai X, Halpert JE, Yang N, Yi L, Zhai J, et al. Accurate Control of Multishelled ZnO Hollow Microspheres for Dye-Sensitized Solar Cells with High Efficiency. *Advanced Materials*. 2012;24(8):1046-9.
28. Xu J, Zhang H, Wang R, Xu P, Tong Y, Lu Q, et al. Delicate Control of Multishelled Zn-Mn-O Hollow Microspheres as a High-Performance Anode for Lithium-Ion Batteries. *Langmuir*. 2018;34(4):1242-8.
29. Tian Q, Zhang F, Yang L. Fabricating thin two-dimensional hollow tin dioxide/carbon nanocomposite for high-performance lithium-ion battery anode. *Applied Surface Science*. 2019;481:1377-84.
30. Mao D, Wan J, Wang J, Wang D. Sequential Templating Approach: A Groundbreaking Strategy to Create Hollow Multishelled Structures. *Advanced Materials*. 2019;31(38):1802874.
31. Xing L-L, Zhao G-G, Huang K-J, Wu X. A yolk-shell V₂O₅ structure assembled from ultrathin nanosheets and coralline-shaped carbon as advanced electrodes for a high-performance asymmetric supercapacitor. *Dalton Transactions*. 2018;47(7):2256-65.
32. Tao J, Zhou J, Yao Z, Jiao Z, Wei B, Tan R, et al. Multi-shell hollow porous carbon nanoparticles with excellent microwave absorption properties. *Carbon*. 2021;172:542-55.
33. Bin D-S, Chi Z-X, Li Y, Zhang K, Yang X, Sun Y-G, et al. Controlling the Compositional Chemistry in Single Nanoparticles for Functional Hollow Carbon Nanospheres. *Journal of the American Chemical Society*. 2017;139(38):13492-8.
34. Zhang P, Guan BY, Yu L, Lou XW. Facile Synthesis of Multi-shelled ZnS-CdS Cages with Enhanced Photoelectrochemical Performance for Solar Energy Conversion. *Chem*. 2018;4(1):162-73.
35. Huang C-C, Huang W, Yeh C-S. Shell-by-shell synthesis of multi-shelled mesoporous silica nanospheres for optical imaging and drug delivery. *Biomaterials*. 2011;32(2):556-64.
36. Liu J, Hartono SB, Jin YG, Li Z, Lu GQ, Qiao SZ. A facile vesicle template route to multi-shelled mesoporous silica hollow nanospheres. *Journal of Materials Chemistry*. 2010;20(22):4595-601.
37. Seljak KB, Kocbek P, Gašperlin M. Mesoporous silica nanoparticles as delivery carriers: An overview of drug loading techniques. *Journal of Drug Delivery Science and Technology*. 2020;59:101906.
38. Lehto VP, Riikonen J. 14 - Drug loading and characterization of porous silicon materials. In: Santos HA, editor. *Porous Silicon for Biomedical Applications*: Woodhead Publishing; 2014. p. 337-55.
39. Ambrogi V, Perioli L, Marmottini F, Giovagnoli S, Esposito M, Rossi C. Improvement of dissolution rate of piroxicam by inclusion into MCM-41 mesoporous silicate. *European Journal of Pharmaceutical Sciences*. 2007;32(3):216-22.
40. Heikkilä T, Salonen J, Tuura J, Kumar N, Salmi T, Murzin DY, et al. Evaluation of Mesoporous TCPSi, MCM-41, SBA-15, and TUD-1 Materials as API Carriers for Oral Drug Delivery. *Drug Delivery*. 2007;14(6):337-47.
41. Datt A, El-Maazawi I, Larsen SC. Aspirin Loading and Release from MCM-41 Functionalized with Aminopropyl Groups via Co-condensation or Postsynthesis Modification Methods. *The Journal of Physical Chemistry C*. 2012;116(34):18358-66.
42. Kanwal F, Ma M, Rehman MFu, Khan F-u, Elizur SE, Batoool AI, et al. Aspirin Repurposing in Folate-Decorated Nanoparticles: Another Way to Target Breast Cancer. *Frontiers in Molecular Biosciences*. 2022;8.
43. Wang Z, Chen B, Quan G, Li F, Wu Q, Dian L, et al. Increasing the oral bioavailability of poorly water-soluble carbamazepine using immediate-release pellets supported on SBA-15 mesoporous silica. *International journal of nanomedicine*. 2012;7:5807-18.
44. Charnay C, Bégu S, Tourné-Péteilh C, Nicole L, Lerner DA, Devoisselle JM. Inclusion of ibuprofen in mesoporous templated silica: drug loading and release property. *European Journal of Pharmaceutics and Biopharmaceutics*. 2004;57(3):533-40.
45. Mellaerts R, Jammaer JAG, Van Speybroeck M, Chen H, Humbeeck JV, Augustijns P, et al. Physical State of Poorly Water Soluble Therapeutic Molecules Loaded into SBA-15 Ordered Mesoporous Silica Carriers: A Case Study with Itraconazole and Ibuprofen. *Langmuir*. 2008;24(16):8651-9.

46. Ambrogi V, Marmottini F, Pagano C. Amorphous carbamazepine stabilization by the mesoporous silicate SBA-15. *Microporous and Mesoporous Materials*. 2013;177:1-7.
47. Ambrogi V, Perioli L, Pagano C, Latterini L, Marmottini F, Ricci M, et al. MCM-41 for furosemide dissolution improvement. *Microporous and Mesoporous Materials*. 2012;147(1):343-9.
48. Homayun B, Lin X, Choi H-J. Challenges and Recent Progress in Oral Drug Delivery Systems for Biopharmaceuticals. *Pharmaceutics*. 2019;11(3):129.
49. Kiptoo P, Calcagno AM, Siahaan TJ. Physiological, Biochemical, and Chemical Barriers to Oral Drug Delivery. *Drug Delivery* 2016. p. 19-34.
50. Vancamelbeke M, Vermeire S. The intestinal barrier: a fundamental role in health and disease. *Expert Rev Gastroenterol Hepatol*. 2017;11(9):821-34.
51. Pollard KM. Silica, Silicosis, and Autoimmunity. *Front Immunol*. 2016;7:97-.
52. Leung CC, Yu ITS, Chen W. Silicosis. *The Lancet*. 2012;379(9830):2008-18.
53. Guo C, Xia Y, Niu P, Jiang L, Duan J, Yu Y, et al. Silica nanoparticles induce oxidative stress, inflammation, and endothelial dysfunction in vitro via activation of the MAPK/Nrf2 pathway and nuclear factor-κB signaling. *International journal of nanomedicine*. 2015;10:1463-77.
54. Duan J, Yu Y, Li Y, Yu Y, Li Y, Zhou X, et al. Toxic effect of silica nanoparticles on endothelial cells through DNA damage response via Chk1-dependent G2/M checkpoint. *PLoS One*. 2013;8(4):e62087-e.
55. Tarantini A, Lancelleur R, Mourot A, Lavault MT, Casterou G, Jarry G, et al. Toxicity, genotoxicity and proinflammatory effects of amorphous nanosilica in the human intestinal Caco-2 cell line. *Toxicology in Vitro*. 2015;29(2):398-407.
56. Ryu HJ, Seong NW, So BJ, Seo HS, Kim JH, Hong JS, et al. Evaluation of silica nanoparticle toxicity after topical exposure for 90 days. *International journal of nanomedicine*. 2014;9 Suppl 2(Suppl 2):127-36.
57. Li L, Liu T, Fu C, Tan L, Meng X, Liu H. Biodistribution, excretion, and toxicity of mesoporous silica nanoparticles after oral administration depend on their shape. *Nanomedicine : nanotechnology, biology, and medicine*. 2015;11(8):1915-24.
58. Lee J-A, Kim M-K, Paek H-J, Kim Y-R, Kim M-K, Lee J-K, et al. Tissue distribution and excretion kinetics of orally administered silica nanoparticles in rats. *International journal of nanomedicine*. 2014;9 Suppl 2(Suppl 2):251-60.
59. Lea T. Caco-2 Cell Line. In: Verhoeckx K, Cotter P, López-Expósito I, Kleiveland C, Lea T, Mackie A, et al., editors. *The Impact of Food Bioactives on Health: in vitro and ex vivo models*. Cham (CH): Springer Copyright 2015, The Author(s). 2015. p. 103-11.
60. Schindelin J, Arganda-Carreras I, Frise E, Kaynig V, Longair M, Pietzsch T, et al. Fiji: an open-source platform for biological-image analysis. *Nat Methods*. 2012;9(7):676-82.
61. Sing K. Reporting Physisorption Data for Gas/Solid Systems with Special Reference to the Determination of Surface Area and Porosity. *Pure and Applied Chemistry - PURE APPL CHEM*. 1982;54:2201-18.
62. Yu L, Zhu Y, Wang Y, Chen S. FRACTAL CHARACTERISTICS OF NANOSCALE PORES IN SHALE AND ITS IMPLICATIONS ON METHANE ADSORPTION CAPACITY. *Fractals*. 2019;27:1940014.
63. Mudalige T, Qu H, Van Haute D, Ansar SM, Paredes A, Ingle T. Chapter 11 - Characterization of Nanomaterials: Tools and Challenges. In: López Rubio A, Fabra Rovira MJ, Martínez Sanz M, Gómez-Mascaraque LG, editors. *Nanomaterials for Food Applications: Elsevier*; 2019. p. 313-53.
64. Su G, Yang C, Zhu J-J. Fabrication of Gold Nanorods with Tunable Longitudinal Surface Plasmon Resonance Peaks by Reductive Dopamine. *Langmuir : the ACS journal of surfaces and colloids*. 2014;31.
65. Laboratories CSH. Phosphate-buffered saline (PBS). *Cold Spring Harbor Protocols*. 2006;2006(1):pdb. rec8247.
66. da Cruz Schneid A, Albuquerque LJC, Mondo GB, Ceolin M, Picco AS, Cardoso MB. Colloidal stability and degradability of silica nanoparticles in biological fluids: a review. *Journal of Sol-Gel Science and Technology*. 2022;102(1):41-62.
67. Arora M. Cell Culture Media: A Review. *Materials and Methods*. 2013;3.
68. Rascol E, Daurat M, Da Silva A, Maynadier M, Dorandeu C, Charnay C, et al. Biological Fate of Fe3O4 Core-Shell Mesoporous Silica Nanoparticles Depending on Particle Surface Chemistry. *Nanomaterials*. 2017;7(7):162.
69. Cauda V, Argyo C, Bein T. Impact of different PEGylation patterns on the long-term bio-stability of colloidal mesoporous silica nanoparticles. *Journal of Materials Chemistry*. 2010;20(39):8693-9.
70. Lin Y-S, Abadeer N, Haynes CL. Stability of small mesoporous silica nanoparticles in biological media. *Chemical Communications*. 2011;47(1):532-4.
71. Croissant JG, Fatieiev Y, Khashab NM. Degradability and Clearance of Silicon, Organosilica, Silsesquioxane, Silica Mixed Oxide, and Mesoporous Silica Nanoparticles. *Advanced Materials*. 2017;29(9):1604634.
72. Hadipour Moghaddam SP, Mohammadpour R, Ghandehari H. In vitro and in vivo evaluation of degradation, toxicity, biodistribution, and clearance of silica nanoparticles as a function of size, porosity, density, and composition. *Journal of Controlled Release*. 2019;311-312:1-15.
73. Braun K, Pochert A, Beck M, Fiedler R, Gruber J, Lindén M. Dissolution kinetics of mesoporous silica nanoparticles in different simulated body fluids. *Journal of Sol-Gel Science and Technology*. 2016;79(2):319-27.
74. Hao N, Liu H, Li L, Chen D, Li L, Tang F. In vitro degradation behavior of silica nanoparticles under physiological conditions. *Journal of nanoscience and nanotechnology*. 2012;12(8):6346-54.
75. Lin P-C, Lin S, Wang PC, Sridhar R. Techniques for physicochemical characterization of nanomaterials. *Biotechnol Adv*. 2014;32(4):711-26.
76. Suttiponparnit K, Jiang J, Sahu M, Suvachittanont S, Charinpanitkul T, Biswas P. Role of Surface Area, Primary Particle Size, and Crystal Phase on Titanium Dioxide Nanoparticle Dispersion Properties. *Nanoscale Res Lett*. 2011;6(1):27-.
77. Kosmulski M. The pH-Dependent Surface Charging and the Points of Zero Charge. *Journal of Colloid and Interface Science*. 2002;253(1):77-87.
78. Nur Y, Lead JR, Baalousha M. Evaluation of charge and agglomeration behavior of TiO2 nanoparticles in

- ecotoxicological media. *Science of The Total Environment*. 2015;535:45-53.
79. Braun K, Stürzel CM, Biskupek J, Kaiser U, Kirchhoff F, Lindén M. Comparison of different cytotoxicity assays for in vitro evaluation of mesoporous silica nanoparticles. *Toxicology in Vitro*. 2018;52:214-21.
80. Chang J-S, Chang KLB, Hwang D-F, Kong Z-L. In Vitro Cytotoxicity of Silica Nanoparticles at High Concentrations Strongly Depends on the Metabolic Activity Type of the Cell Line. *Environmental Science & Technology*. 2007;41(6):2064-8.
81. Gehrke H, Frühmesser A, Pelka J, Esselen M, Hecht LL, Blank H, et al. In vitro toxicity of amorphous silica nanoparticles in human colon carcinoma cells. *Nanotoxicology*. 2012;7(3):274-93.
82. Pizzino G, Irrera N, Cucinotta M, Pallio G, Mannino F, Arcoraci V, et al. Oxidative Stress: Harms and Benefits for Human Health. *Oxid Med Cell Longev*. 2017;2017:8416763-.
83. Sun L, Li Y, Liu X, Jin M, Zhang L, Du Z, et al. Cytotoxicity and mitochondrial damage caused by silica nanoparticles. *Toxicology in Vitro*. 2011;25(8):1619-29.
84. Alkhamash HI, Li N, Berthier R, de Planque MRR. Native silica nanoparticles are powerful membrane disruptors. *Physical Chemistry Chemical Physics*. 2015;17(24):15547-60.
85. Fröhlich E, Samberger C, Kueznik T, Absenger M, Roblegg E, Zimmer A, et al. Cytotoxicity of nanoparticles independent from oxidative stress. *The Journal of toxicological sciences*. 2009;34(4):363-75.
86. Halamoda-Kenzaoui B, Ceridono M, Colpo P, Valsesia A, Urbán P, Ojea-Jiménez I, et al. Dispersion Behaviour of Silica Nanoparticles in Biological Media and Its Influence on Cellular Uptake. *PLoS One*. 2015;10(10):e0141593-e.
87. Cho EC, Zhang Q, Xia Y. The effect of sedimentation and diffusion on cellular uptake of gold nanoparticles. *Nat Nanotechnol*. 2011;6(6):385-91.
88. Foroozandeh P, Aziz AA. Insight into Cellular Uptake and Intracellular Trafficking of Nanoparticles. *Nanoscale Res Lett*. 2018;13(1):339.
89. Nan A, Bai X, Son SJ, Lee SB, Ghandehari H. Cellular Uptake and Cytotoxicity of Silica Nanotubes. *Nano Letters*. 2008;8(8):2150-4.

Supplementary Information

In vitro cytotoxicity

Metabolic activity (%) in the MTT assay and ROS production (%) in the H₂DCFDA assay were determined relative to a non-exposed control using the following formulas:

$$\text{Relative metabolic activity (\%)} = 100 \times \frac{\text{Absorbance}_{\text{exposed cells}}}{\text{Absorbance}_{\text{control cells}}}$$

$$\text{Relative ROS production (\%)} = 100 \times \frac{\text{Fluorescence}_{\text{exposed cells}}}{\text{Fluorescence}_{\text{control cells}}}$$

Cytotoxicity (%) in the LDH assay was determined by the following formula:

$$\text{Cytotoxicity (\%)} = 100 \times \frac{\text{Absorbance}_{\text{exposed cells}} - \text{Absorbance}_{\text{control cells}}}{\text{Absorbance}_{\text{maximum LDH release cells}} - \text{Absorbance}_{\text{control cells}}}$$

and subsequently compared to the non-exposed control to obtain relative cytotoxicity values (%):

$$\text{Relative cytotoxicity (\%)} = 100 \times \frac{\text{Cytotoxicity}_{\text{exposed cells}}}{\text{Cytotoxicity}_{\text{control cells}}}$$

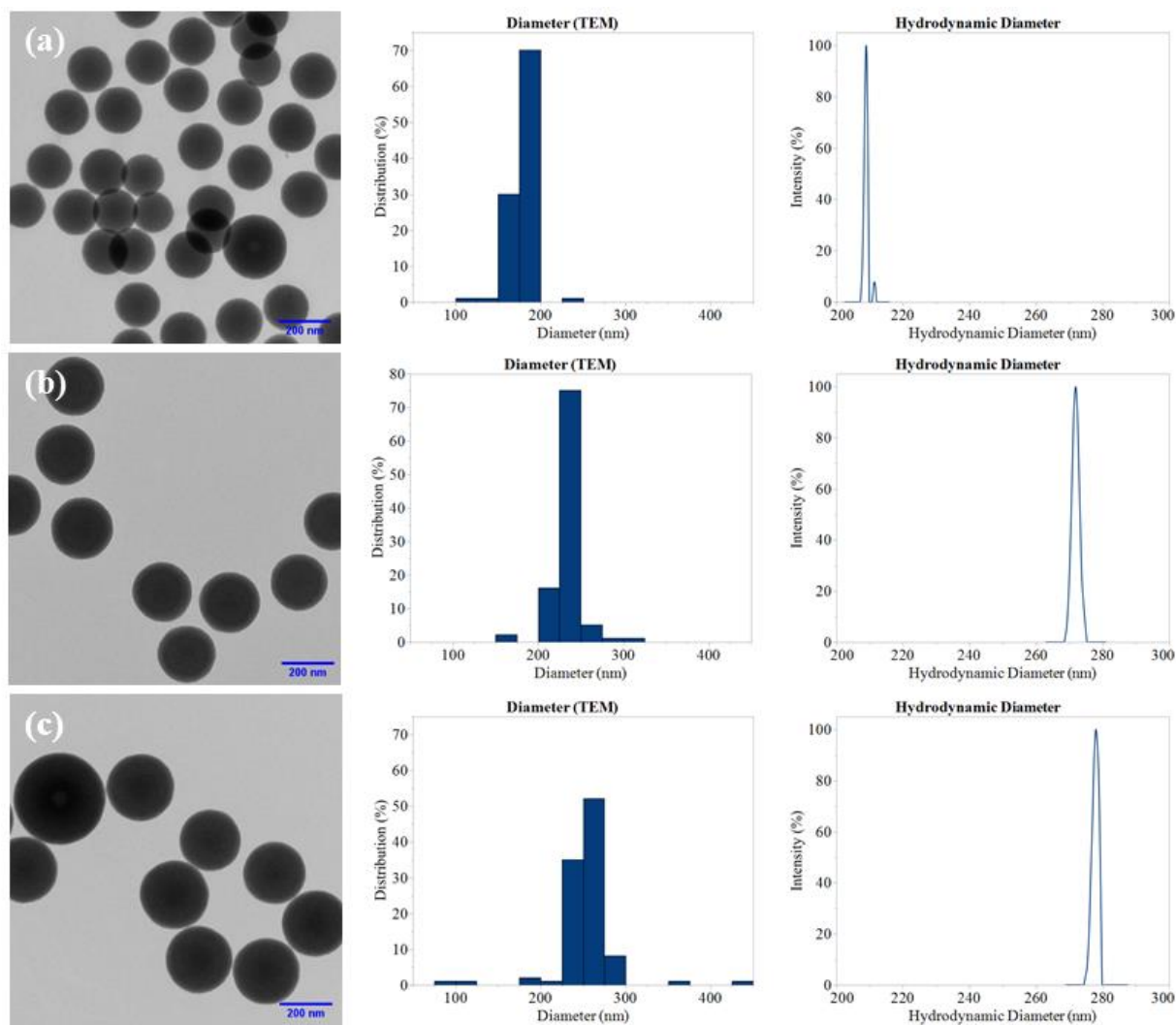


Fig. S1. TEM images of the single-layer PMOs exposed to a solvothermal treatment in ethanol. Various precursor contents of (a) 150, (b) 250, or (c) 350 $\mu\text{l}/\text{layer}$ were used during the synthesis. The diameter of the PMOs was determined based on a minimum of 100 particles per sample as visualized by TEM. The average diameter (nm) for each sample was 177 ± 12 nm, 234 ± 17 nm, and 256 ± 37 nm respectively. The hydrodynamic diameter (nm) was determined using DLS of the sample dispersed in water (Millipore, 1 mg/ml). The hydrodynamic diameter with the highest intensity for each sample was 204.3 nm, 247.1 nm, and 278.0 nm respectively, averaging at a hydrodynamic diameter of 200 ± 20 nm, 247 ± 1 nm, and 278 ± 1 nm respectively. The PDI for each sample was 0.036, 0.005, and 0.036 respectively.

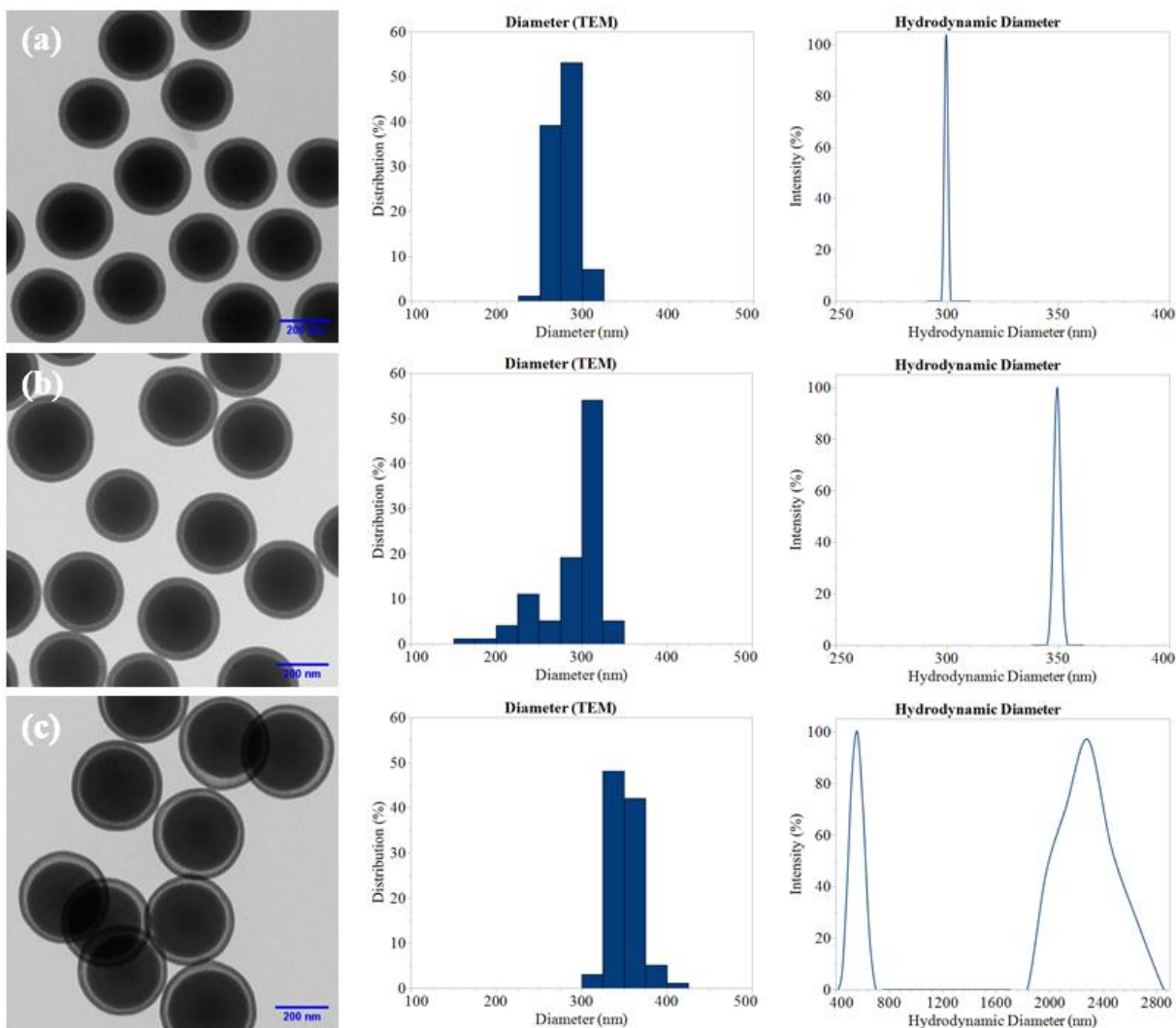


Fig. S2. TEM images of the double-layer PMOs exposed to a solvothermal treatment in ethanol. Various precursor contents of (a) 150, (b) 250, or (c) 350 µl/layer were used during the synthesis. The diameter of the PMOs was determined based on a minimum of 100 particles per sample as visualized by TEM. The average diameter (nm) for each sample was 279 ± 13 nm, 276 ± 39 nm, and 352 ± 41 nm respectively. The hydrodynamic diameter (nm) was determined using DLS of the sample dispersed in water (Millipore, 1 mg/ml). The hydrodynamic diameter with the highest intensity for each sample was 301 nm, 350 nm, and 561 nm respectively, averaging at a hydrodynamic diameter of 300 ± 1 nm, 350 ± 2 nm, and 554 ± 49 nm respectively. An additional high intensity peak can be observed in (c) at 2287 nm, indicating agglomeration of the PMOs. The PDI for each sample was 0.005, 0.017, and 0.270 respectively.

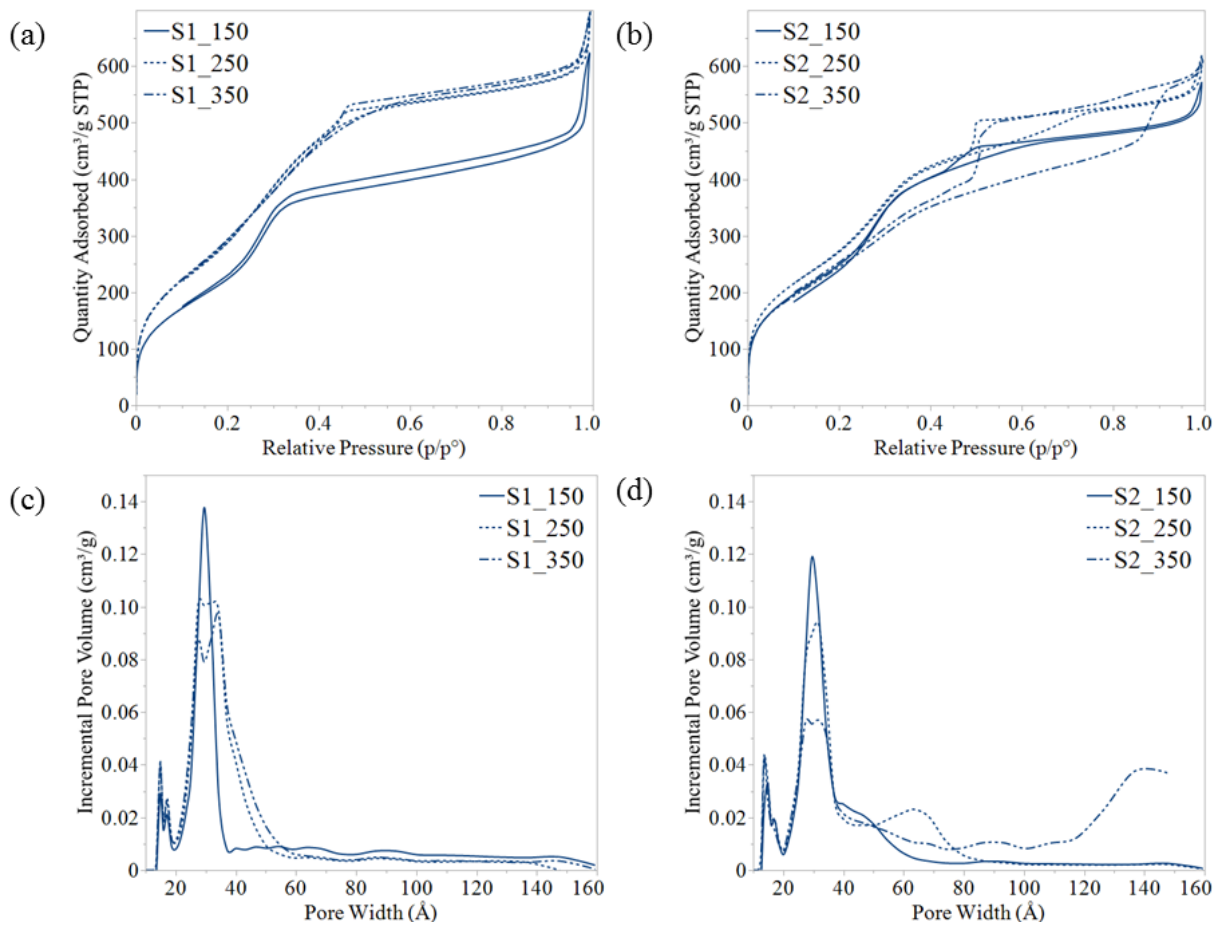


Fig. S3. Nitrogen sorption isotherms (a-b) and pore size distribution (c-d) are given for the (a,c) single, and (b,d) double-layer PMOs, exposed to a solvothermal treatment.

Table S1. Nitrogen sorption results.

Sample	S_{BET} (m ² /g)	V_{Total} (cm ³ /g)	$V_{Adsorption}$ (cm ³ /g)	$V_{Desorption}$ (cm ³ /g)
S _{1_350}	1192	1.08	0.78	0.92
S _{1_250}	1147	1.08	0.76	0.90
S _{1_150}	919	0.97	0.62	0.73
S _{2_350}	946	0.95	0.71	0.92
S _{2_250}	1066	0.96	0.72	0.89
S _{2_150}	969	0.89	0.67	0.79

S_{BET} was estimated using the Brunauer-Emmett-Teller (BET) method, V_{total} was estimated with Barrett-Joyner-Halenda (BJH) analysis using data at a relative pressure (p/p^0) > 0.99.

Sample: S_{[# layers]_[total precursor content (μl)]}.

S_{BET} : specific surface area; V_{Total} : total pore volume.

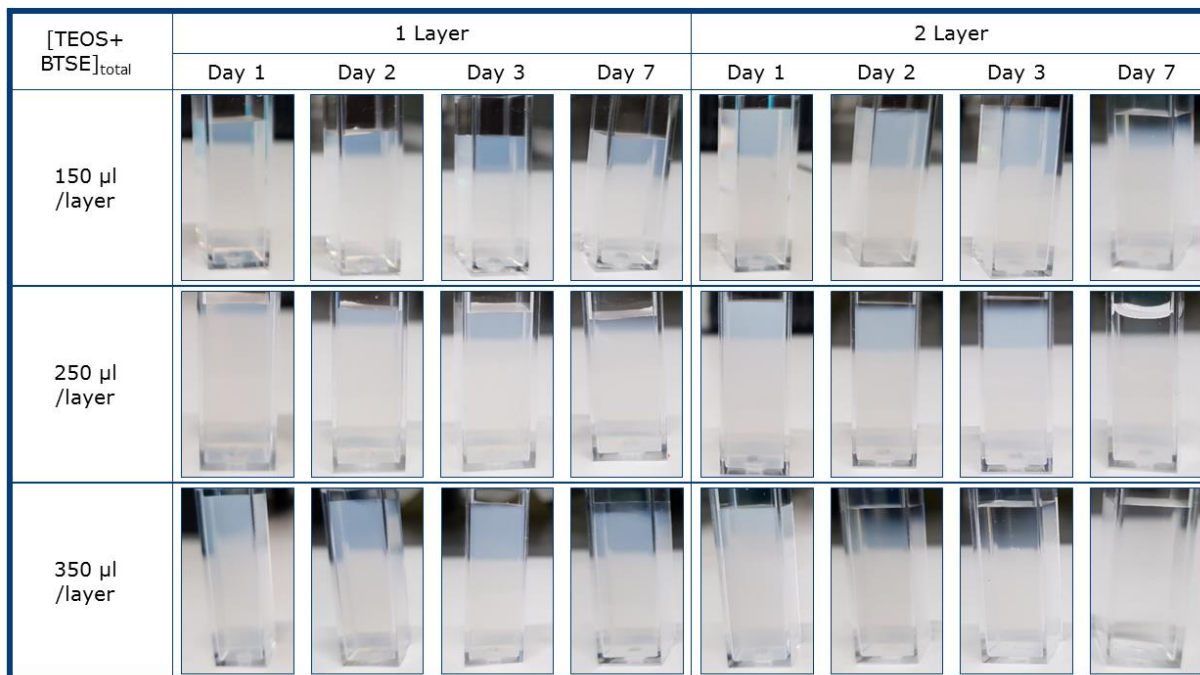


Fig. S4. Nanoparticle sedimentation of PMOs with exposure to a solvothermal treatment. The PMOs were dispersed in water (Millipore, 1 mg/ml) and left to sediment for a week. On day 1 all solutions were turbid. Solutions containing PMOs with more layers and/or a higher precursor content per layer became less turbid over multiple days, indicating sedimentation, while other solutions stayed relatively turbid, indicating dispersed samples.

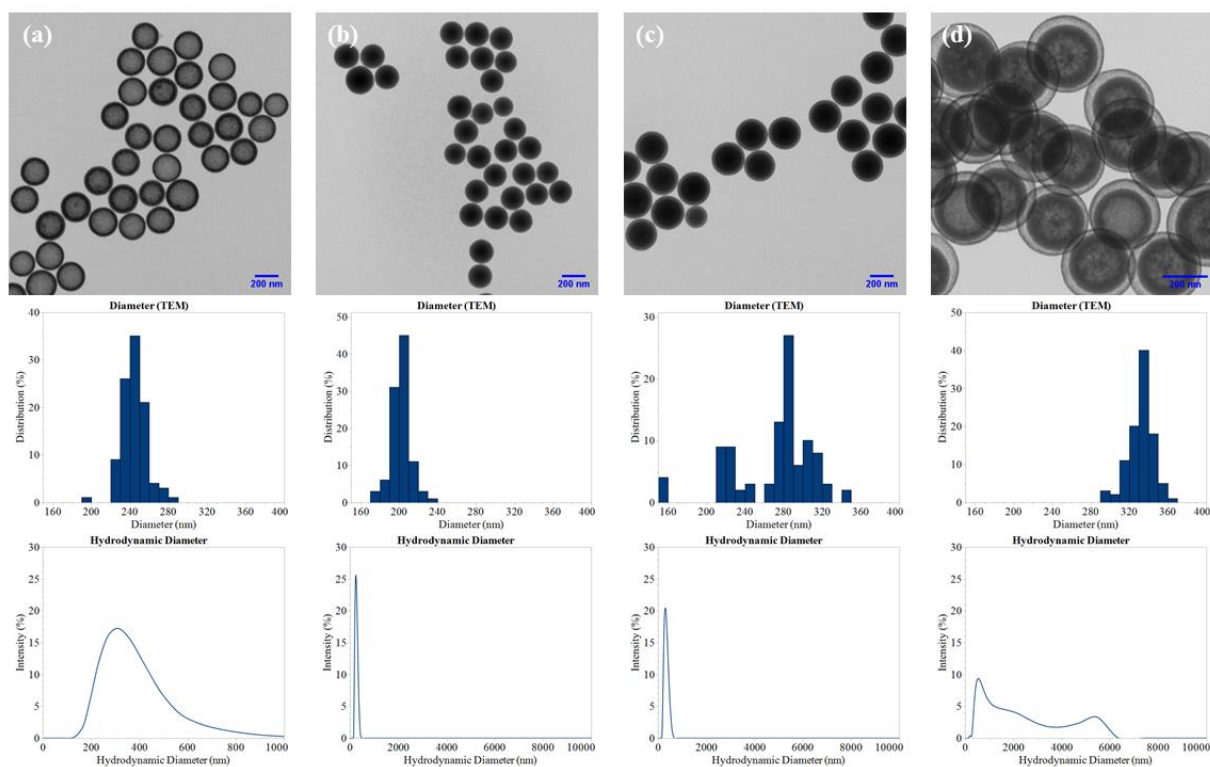


Fig. S5. (a) TEM image and size distribution of C₁ PMOs. The C₁ PMOs had a diameter of 202 ± 10 nm and a hydrodynamic diameter of 260 ± 3 nm. (b) TEM image and size distribution of H₁ PMOs. The PMOs had a diameter of 245 ± 13 nm and a hydrodynamic diameter of 350 ± 15 nm. (c) TEM image and size distribution of S₂ PMOs. The PMOs had a diameter of 272 ± 39 nm and a hydrodynamic diameter of 304 ± 31 nm. (d) TEM image and size distribution of H₂ PMOs. The PMOs had a diameter of 332 ± 13 nm and a hydrodynamic diameter of 478 ± 5 nm. The diameter of the nanoparticles was determined based on a minimum of 100 particles per sample as visualized by TEM. The hydrodynamic diameter (nm) was determined using DLS of the sample dispersed in water (Millipore, 1 mg/ml).

Table S2. Size of the selected nanoparticles as determined by TEM and DLS.

Sample	Diameter (nm)	Hydrodynamic Diameter (nm)	PDI	IEP
C ₁	202 ± 10	260 ± 3	0.045	3.0
S ₂	272 ± 39	304 ± 31	0.066	3.0
H ₁	245 ± 13	350 ± 15	0.190	3.5
H ₂	332 ± 13	479 ± 5	0.102	5.0

Diameters (nm) were determined using TEM and are given as mean ± SD; hydrodynamic diameters (nm) were determined using MADLS and are given as mean ± SD; IEPs were determined based on the zeta potential measurements of the two lowest pH measurements.

TEM: transmission electron microscopy; MADLS: multi-angle dynamic light scattering; PDI: polydispersity index; IEP: isoelectric point.

Table S3. Nitrogen sorption results of selected nanoparticles.

Sample	S _{BET} (m ² /g)	V _{Total} (cm ³ /g)	V _{Adsorption} (cm ³ /g)	V _{Desorption} (cm ³ /g)
C ₁	1090	0.791	0.237	0.370
S ₂	1015	0.907	0.689	0.855
H ₁	517	0.618	0.338	0.385
H ₂	617	0.922	0.406	0.849

S_{BET} was estimated using the Brunauer-Emmett-Teller (BET) method, V_{total} was estimated with Barrett-Joyner-Halenda (BJH) analysis using data at a relative pressure (p/p⁰) > 0.99.

S_{BET}: surface area; V_{Total}: pore volume.

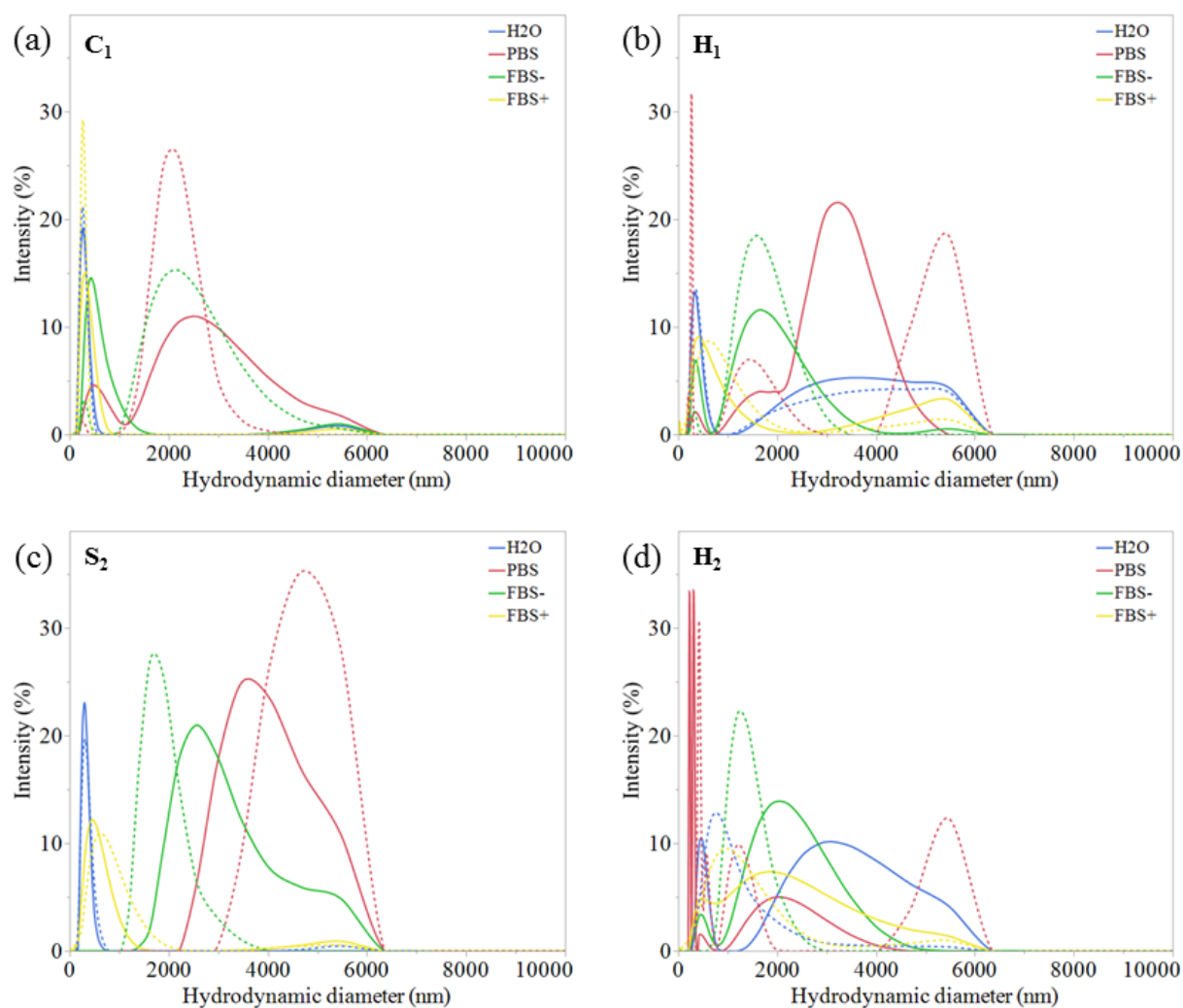


Fig. S6. Hydrodynamic diameter (nm) distribution of (a) C₁ PMOs, (b) H₁ PMOs, (c) S₂ PMOs, and (d) H₂ PMOs in various media (H₂O, PBS, cell culture medium without FBS, and cell culture medium with FBS). Distributions with a solid line were measured immediately after ultra-sonication. Distributions with a dotted line were measured 24 hours after the initial measurement.